This is a preprint, the final version is subject to change, of the American Mineralogist (MSA)
Cite as Authors (Year) Title. American Mineralogist, in press.
(DOI will not work until issue is live.) DOI: http://dx.doi.org/10.2138/am-2017-6053

REVISON 1

Geochemistry of the Cretaceous Kaskanak Batholith and Genesis of the Pebble Porphyry Cu-Au-Mo deposit, Southwest Alaska

by

Olson, Nansen H., Dilles, John H., Kent, Adam J.R., Oregon State University, Corvallis, OR, USA
Lang, James R., Hunter Dickinson, Vancouver, British Colombia, Canada

A submission to *American Mineralogist, special volume – From Magmas to Ore Deposits*
Corresponding Author: olsonn@oregonstate.edu

Abstract

The key magmatic processes that lead to the formation of large magmatic-hydrothermal porphyry copper mineral deposits remain uncertain, and a particular question is why a few of these deposits, such as the Pebble porphyry Cu-Au-Mo deposit, are strongly enriched in both gold and molybdenum. This study investigated the igneous rocks of the Pebble district and obtained major and trace element compositions, Sr and Nd isotopic compositions, and zircon age and trace element data in order to model the origin of the ore-forming magmas.

The Pebble porphyry Cu-Au-Mo deposit, one of the world's largest Cu-Au resources, formed during the final stages of regional Late Cretaceous arc magmatism (101-88 Ma) in the Southwest Alaska Range. Local pre-mineral intrusions (99-95 Ma) are dominated by alkaline compositions including monzodiorite stocks, shoshonite dikes, and monzonite porphyries, but also include lesser volumes of high-K calc-alkaline diorite and granodiorite sills. The occurrence of early alkaline magmas has been noted at other gold-rich porphyry systems, including Bingham and Kerr-Sulphurets-Mitchell. Mineralization at Pebble is associated with granodiorite to granite porphyry dikes related to the >165 km^2 high-K calc-alkaline Kaskanak granodiorite batholith

This is a preprint, the final version is subject to change, of the American Mineralogist (MSA)
Cite as Authors (Year) Title. American Mineralogist, in press.
(DOI will not work until issue is live.) DOI: http://dx.doi.org/10.2138/am-2017-6053

(91-89 Ma). Over a period of 10 m.y., Late Cretaceous melts evolved from high temperatures (930-730˚C) and modestly hydrous and oxidized conditions to relatively low temperatures (760-680˚C) and very hydrous and oxidized conditions. Collectively, all Late Cretaceous igneous rocks at Pebble contain magnetite and little or no ilmenite, are metaluminous to weakly peraluminous, and have typical arc trace element enrichments and depletions. They have moderate Sr/Y ratios (20 – 55) and gently sloped REE profiles (La/Yb = 5 – 20) that are not adakitic, which supports a source area lacking garnet that is consistent with a thin crust in southwest Alaska.

Radiogenic isotopes for Late Cretaceous intrusions at Pebble have a restricted range of primitive Sr and Nd isotopic compositions ($^{87}Sr/^{86}Sr_i$ = 0.70329 - 0.70424; εNd_i = +4.9 - +6.1 calculated at 90 Ma), which overlap with volcanic and plutonic basement rocks of the Jurassic Talkeetna Arc along the Alaska Peninsula. The Kaskanak batholith intrudes the Late Jurassic – Early Cretaceous Kahiltna flysch, and mixing models using Sr and Nd isotopes indicate that the Kaskanak batholith assimilated ≤10 wt.% Kahiltna flysch in amounts that did not likely affect magma fertility. Xenocrystic zircons are abundant in Cretaceous pre-mineral intrusions and have U-Pb ages similar to detrital zircons in the Kahiltna flysch. These data support some assimilation of upper crustal Kahiltna flysch, but the dominance of Devonian – Mississippian xenocrystic zircon populations in some intrusions suggests derivation from unexposed older basement.

The extraordinary endowment of Cu and Au at Pebble is inferred to result from primitive calc-alkaline and alkaline arc magmas and the hydrous and strongly oxidized conditions that suppressed the formation and fractionation of Cu- and Au-enriched sulfide melts. Furthermore, differentiation to silicic compositions was a product of extensive crystal fractionation of parental melts accompanied by minor crustal assimilation. The trace element content of the intermediate

This is a preprint, the final version is subject to change, of the American Mineralogist (MSA)
Cite as Authors (Year) Title. American Mineralogist, in press.
(DOI will not work until issue is live.) DOI: http://dx.doi.org/10.2138/am-2017-6053

composition intrusions indicates that both hornblende and titanite fractionation processes in the mid- to shallow-crust were both required to produce the more evolved granodiorite and granite porphyry compositions. Despite the apparent lack of Mo-enriched continental crust in the region, primitive hydrous melts were produced by protracted arc magmatism and were modified by minor crustal assimilation including early alkaline magmatism, periodic recharge of mafic hydrous basalts and hybrid andesites, and fractional crystallization which was apparently sufficient to enrich Mo in late stage felsic melts.

Introduction

The Pebble porphyry Cu-Au-Mo deposit in southwest Alaska (Fig. 1) is one of the world's largest Cu-Au-Mo-Ag mineral resources with 10.9 Bt ore containing 36.9 Mt copper, 2.53 Mt molybdenum, 3,054 t gold, and 13,488 t silver, as well as abundant rhenium and minor palladium (Lang et al., 2013; Rebagliati and Lang, 2015). Late Cretaceous magmatism of the Southwest (SW) Alaska Range belt (Fig.1; Young et al., 1997; Hart et al., 2004; Goldfarb et al., 2013) spanned ~10 m.y. in the Lake Iliamna region and culminated with the intrusion of the Kaskanak batholith that consists largely of equigranular granodiorite and small volumes of granodiorite to granite porphyry dikes associated with ore formation.

Previous studies on the Pebble deposit have documented the geology and age of intrusions and ores (Bouley et al., 1995; Schrader, 2001; Ricardo, 2009; Gaunt et al., 2010; Lang et al., 2013; Olson, 2015), interpretations from regional-scale aeromagnetic data (Anderson et al., 2014), the mineralogy, geochemistry, and fluid-inclusion characteristics of hydrothermally altered rocks (Gregory et al., 2013; Harraden et al., 2013; Gregory, 2017), and the radiogenic isotope characteristics of intrusions in the district (Ayuso et al., 2013; Goldfarb et al., 2013). In

This is a preprint, the final version is subject to change, of the American Mineralogist (MSA)
Cite as Authors (Year) Title. American Mineralogist, in press.
(DOI will not work until issue is live.) DOI: http://dx.doi.org/10.2138/am-2017-6053

this contribution, we expand the petrological and geochemical data for magmatism in the Pebble district and include barren pre-ore calc-alkaline sills, pre-ore alkaline intrusions, the mineralized Kaskanak batholith, and post-ore Paleocene and Eocene hypabyssal dikes and intrusions. We examine the whole-rock major and trace elements, whole-rock Sr-Nd isotopic compositions, and rare earth element (REE) abundances of zircon and titanite from intrusions in the district to constrain the source of magmas and the role of assimilation and fractional crystallization (AFC) processes in generating the ore-forming magmas. Finally, we conclude with a discussion of the origin of the extraordinary metal endowment of Cu, Au, and Mo at Pebble and the likely key igneous processes that produced water, chloride, sulfur, and metal-rich melts from which ore fluids were extracted.

Geochemical appraisals of arc magmas

Recent studies have developed many semi-quantitative geochemical techniques for assessing fertility of volcanic arc magmas on the basis of oxidation and hydration of the melt. In fertile volcanic arcs, parental magmas of large porphyry deposits are necessarily water-rich (>2.5 wt.%, typically ≥4 wt.%), oxidized (e.g., often $\geq\Delta$NNO+2) , rich in halogens (e.g., $Cl/H_2O \geq 0.5$), anomalous in sulfur (e.g., $Fe/S \leq 100$), and have experienced significant crystal-fractionation in order to increase chalcophile metal partitioning from the melt to the hydrothermal system (Burnham and Ohmoto, 1980; Candela and Holland, 1986; Dilles, 1987; Cline and Bodnar, 1991; Webster, 1992; Candela, 1992; Candela and Piccoli, 2005; Richards, 2011; Dilles et al., 2015). Redox sensitive proxies, such as Ce and Eu anomalies in zircon (Ballard et al., 2002; Trail et al., 2011; Dilles et al., 2015) or whole-rock V/Sc ratios (Loucks,

2014) have also been utilized to infer oxidized conditions where Fe-Ti oxides are not present or preserved.

The petrographic context of these magmas is also critical for constraining and interpreting these geochemical proxies. For example, the presence of titanite in equilibrium with magnetite and quartz suggests highly oxidized melts (e.g., ≥ΔNNO+2, Dilles, 1987; Wones, 1989), and the presence of amphibole suggests minimum magmatic water contents of 3.5 wt.% H_2O for granodiorite compositions at shallow crustal pressures (Naney, 1983). The presence of amphibole and/or titanite can also greatly impact the high field strength element (HFSE) and rare earth element (REE) budget of differentiated melts (e.g., Kay and Mpodozis, 2001; Richards and Kerrich, 2007; Glazner et al., 2008; Bachmann and Bergantz, 2008). Several workers (Seedorff et al., 2005; Richards and Kerrich, 2007; Chiaradia et al., 2009; Richards, 2011; Richards et al., 2012; Loucks, 2014) have advocated the importance of high water content in producing typical geochemical features of porphyry copper deposits and other hydrous arc magmas. Richards and Kerrich (2007) suggest high Sr/Y and La/Yb ratios in hydrous arc magmas are likely achieved by amphibole ± titanite fractionation. Amphibole fractionation prevails at near-liquidus (high) temperatures because elevated water contents suppress plagioclase crystallization. These geochemical ratios are accentuated in thicker crust, but are also apparent, albeit less so, in thin crustal settings such as oceanic arcs (Richards and Kerrich, 2007).

Geologic Setting of Southwest Alaska

During the Jurassic to Early Cretaceous, the allochthonous Jurassic – Pennsylvanian Wrangellia composite terrane (WCT; Plafker et al., 1989) of oceanic arc affinity accreted to the North American plate and now makes up the bulk of southern Alaska (Fig. 1). In south-central

This is a preprint, the final version is subject to change, of the American Mineralogist (MSA)
Cite as Authors (Year) Title. American Mineralogist, in press.
(DOI will not work until issue is live.) DOI: http://dx.doi.org/10.2138/am-2017-6053

and southeastern Alaska, the WCT consists of the Peninsular, Wrangellia, and Alexander terranes, whereas in the southwest Alaska only the Peninsular terrane is recognized. In southwestern Alaska, the suture zone between the Peninsular terrane and rocks of continental crustal affinity belonging to the Neoproterozoic – Paleozoic Farewell terrane, a part of the Intermontane belt superterrane, is obscured by younger sedimentary and igneous rocks and is therefore poorly delineated. Basement exposures of the Peninsular terrane consist of sedimentary formations (e.g., Triassic Kamishak and Jurassic Talkeetna Formations) and variably metamorphosed plutonic and volcanic rocks of the Triassic Chilikadrotna Greenstones (flood basalts), other Triassic mafic and ultramafic intrusions (e.g., those from the Tlikakila Complex), and Jurassic intrusive and volcanic rocks of the Talkeetna Arc (Detterman and Reed, 1980). Syn- to post-collisional volcaniclastic flysch deposits up to 5-7 km thick (Kalbas et al., 2007) overlie these basement rocks and were deposited in foreland basins in the Jurassic to Late Cretaceous (Csejtey et al., 1982; Jones et al., 1982; 1986; Coney and Jones, 1985; Wallace et al., 1989; Kalbas et al., 2007; Hampton et al., 2010; Hults et al., 2013). In south-central and southwestern Alaska, these sedimentary strata are informally known as the Kahiltna flysch, noting that the southwestern-most portion of the basin is also known as the Koksetna River Sequence (e.g., Wallace et al, 1989). These sedimentary rocks comprise pelagic shales and turbidites of fine- to coarse-grained sandstones, siltstones, and minor pebble conglomerates composed of predominantly mafic to intermediate volcanic rock fragments with varying amounts of plagioclase, quartz, clinopyroxene, hornblende, epidote, and sedimentary rock fragments (Plafker et al., 1989; Wallace et al., 1989).

Concurrent with the development of flysch deposits but farther east in the Eastern Alaska Range, plutons of the Early Cretaceous Chisana arc (Barker, 1987) intruded the Alexander and

Wrangellia terranes (Fig. 1). The early part of this magmatic arc includes the Tosina-St. Elias belt (120-140 Ma), which occurs on the seaward margin of the WCT and contains no known porphyry occurrences. By approximately 120 Ma, Early Cretaceous magmatism had migrated northward to the landward margin of the WCT to form the Nutzotin-Kluane plutonic belt (104-118 Ma) that contains several minor porphyry deposits (Hart et al., 2004; Goldfarb et al., 2013). In the Late Cretaceous (101-88 Ma), intermediate to felsic intrusions of the SW Alaska Range plutonic belt were emplaced in the Western Talkeetna Mountains and Alaska Peninsula (Reed and Lanphere, 1972; Detterman and Reed, 1980; Young et al., 1997; Iriondo et al., 2003; Hart et al., 2004; Amato et al., 2007b; Goldfarb et al., 2013). The SW Alaska Range belt contains few known porphyry copper occurrences, but does include the giant Pebble porphyry deposit.

The SW Alaska Range belt consists predominantly of plutonic rocks and hypabyssal dikes (Reed and Lanphere, 1972; Detterman and Reed, 1980; Amato et al., 2007b) that intrude the Kahiltna flysch and the underlying Kamishak and Talkeetna formations of the Peninsular terrane (Detterman et al., 1996). Paleocene and Eocene volcanic rocks and Quaternary glacial sedimentary rocks are widespread in the SW Alaska Range and unconformably overlie and obscure Mesozoic rocks in the region.

Geology of the Pebble District

In the Pebble district (Fig. 2), Late Cretaceous plutonic rocks span a 10 m.y. period that culminated with emplacement of porphyry dikes and stocks that are genetically linked to the formation of the Pebble porphyry Cu-Au-Mo deposit (see Olson (2015) for a complete chronological summary). Exposures and drill intercepts indicate a >300 km^2 extent of Late Cretaceous plutonic rocks at Pebble, and some workers have suggested aeromagnetic data

This is a preprint, the final version is subject to change, of the American Mineralogist (MSA)
Cite as Authors (Year) Title. American Mineralogist, in press.
(DOI will not work until issue is live.) DOI: http://dx.doi.org/10.2138/am-2017-6053

167 indicate an even larger extent (~900 km^2) beneath volcanic and sedimentary cover (Anderson et
168 al., 2014), thereby making it one of a few large Cretaceous plutonic complexes delineated in the
169 SW Alaska Range belt (Wilson et al., 2015). In the Pebble district, these intrusions are hosted by
170 Early Cretaceous deposits of the Kahiltna flysch based on inherited zircons and crosscutting
171 relationships (Lang et al., 2013). The oldest exposures of igneous rocks in the district include
172 greenschist facies metabasalt and metagabbro roof pendants in the Kaskanak batholith, which
173 likely represent Triassic – Jurassic basement rocks.

174 Pre-mineralization intrusions (ca 99-95 Ma) are precursory to the emplacement of the
175 Kaskanak batholith and are subdivided into two diverse magmatic suites: 1) calc-alkaline sills,
176 and 2) alkalic stocks and porphyry dikes (Bouley et al., 1995; Schrader, 2001; Gaunt et al., 2010;
177 Hart et al., 2010; Lang et al., 2013). Biotite pyroxenite cumulate rocks (~96 Ma) occur with
178 alkalic intrusive rocks in the 25 Zone primarily west of the ZG fault trace (Fig. 2) and may
179 represent the eroded roots of the alkalic magmatic system. There are no known intrusions with
180 ages between 95 and 91 Ma in the district.

181 The Kaskanak batholith (91-89 Ma) is composed of calc-alkaline granodiorite, lesser
182 granite and subordinate andesite intrusions genetically linked to multiple centers of porphyry
183 copper and skarn mineralization. It includes at least three generations of weakly to strongly
184 mineralized granodiorite to granite porphyry dikes and plugs (Fig. 2). The outlined resource
185 boundary of the Pebble deposit includes two main mineralization centers known as the West
186 Zone and East Zone (Fig. 3).

187 Late Cretaceous intrusions were exhumed to the surface in the latest Cretaceous, crosscut
188 by a series of latest Late Cretaceous to Paleocene hypabyssal intrusions (ca 67-58 Ma), and
189 overlain by Paleocene (≤61 Ma; Olson, 2015) volcaniclastic and tuffaceous strata. These

This is a preprint, the final version is subject to change, of the American Mineralogist (MSA)
Cite as Authors (Year) Title. American Mineralogist, in press.
(DOI will not work until issue is live.) DOI: http://dx.doi.org/10.2138/am-2017-6053

previously unnamed hypabyssal intrusions and volcaniclastic sedimentary rocks are herein referred to as the Talarik Intrusive Suite and the Talarik Formation. These rocks may be correlative with the Copper Lake Formation (Detterman and Reed, 1980; Detterman et al., 1996) and similar volcanic and volcaniclastic rocks described in the Dillingham Quadrangle (Iriondo et al., 2003; Wilson et al., 2003). Eocene hypabyssal intrusions and associated volcanic rocks (47-41 Ma) are exposed primarily on the east side of the district around Koktuli Mountain and are henceforth referred to as the Koktuli Intrusive Suite and the Koktuli Volcanics. These Eocene igneous rocks are likely part of the Eocene to earliest Miocene Meshik Arc (Wilson et al., 1985; 2015). Some centers of epithermal mineralization in the district (Fig. 2) are associated with Eocene latite dikes (Fig. 3b; Bouley et al., 1995).

The structural history of the Pebble district is complex. Geologic observations indicate that extension, tilting, and normal faulting occurred during deposition of the Talarik Formation and the Koktuli Volcanics (Olson, 2015). The northeast-striking ZG Fault bounds the western side of the East Graben, has the largest observed offsets, and is one of the oldest normal faults recognized in the district (Fig. 2 and Fig. 3; Olson, 2015). Eocene and younger hypabyssal intrusions and orthogonal normal faulting dissect the ZG fault (Olson, 2015). Collectively, normal faulting in the district has produced approximately 20° eastward rotation (Fig. 3).

Analytical Methods

Whole-rock analyses

In total, 108 whole-rock major and trace element analyses were performed at Washington State University's (WSU) GeoAnalytical Lab using both XRF (Johnson et al., 1999) and ICP-MS methods (Knaack et al., 1994). These samples were collected from drill core and, to the

213 extent possible, were selected to minimize the effects of hydrothermal alteration. For many
214 alteration-sensitive plots (e.g., A/NCK, Sr, etc.), additional samples were culled using Ishikawa
215 alteration index (AI) values ≥ 60 (Ishikawa, 1976; Large et al., 2001; AI = molar
216 100*[K_2O+MgO]/[K_2O+MgO+Na_2O+CaO]) and LOI values ≥ 3.5 wt.%. See Appendix A for
217 the complete whole-rock major and trace element compositions and sample locations. Strontium
218 and neodymium isotopic compositions were determined for 12 samples at the University of Cape
219 Town, South Africa using methods described by Míková and Denková (2007). Appendix A and
220 Table 2 provide additional analytical details.
221
222 **In-situ zircon and titanite analyses**
223 Ten zircon separates were analyzed by the Sensitive High Resolution Ion-Microprobe in
224 reverse geometry (SHRIMP-RG) at the Stanford USGS Micro Analysis Center (SUMAC) to
225 obtain U/Pb age and trace element compositions (Appendix B). Spot sizes for individual analyses
226 were approximately 25 μm diameter and 1-2 μm deep allowing for sampling of high-uranium
227 zones while avoiding cracks, apatite inclusions, and melt inclusions (Mazdab and Wooden,
228 2006). ^{207}Pb-corrected ^{206}Pb/^{238}U spot ages were standardized using the R33 age standard with an
229 assigned age of 420 Ma (Mattinson, 2005). Trace element data were standardized to the MAD
230 and MADDER zircon reference standards of similar composition developed by the SUMAC
231 Laboratory (Mazdab and Wooden, 2006; Wooden and Barth, 2010).
232 An additional 22 zircon separates and 3 samples of titanite from igneous rocks were
233 analyzed by laser ablation inductively-coupled plasma mass spectrometry (LA-ICP-MS) in the
234 W.M. Keck Collaboratory at Oregon State University in order to obtain U/Pb ages and trace
235 element compositions (Appendix C). A Photon Machines Analyte G2 193 nm laser and a

Thermo XseriesII Quadrupole mass spectrometer equipped with an ion counter were used for ICP-MS analyses. Ablation spot diameters ranged between 30 and 40 μm in zircon and were 50 μm in titanite. ^{207}Pb-corrected ^{206}Pb/^{238}U spot ages were standardized using the R33 age standard with an assigned age of 420 Ma (Mattinson, 2005). Reproducibility indicated by the relative percent of the standard error of the mean (SE%) of the R33 standard for N=6 to N=9 analyses on 17 analytical sessions ranges from ±0.8% to ±2.0%. Analyses of a secondary age standard, TEMORA 1 (416.8±1.1 Ma; Black et al., 2003), treated as unknowns and analyzed over the 17 analytical sessions (N=51) produce a mean age of 421.6 Ma with a SE of 2.8 m.y. which overlaps the reported age at the 95% confidence level. Zircon trace element data were processed using in-house LaserTram software (Loewen and Kent, 2012). Zircon data were rigorously screened to remove analyses that encountered apatite inclusions by monitoring for elevated phosphorous and light rare earth element contents. Zircon trace element data were standardized to NIST-612 glass for Nb, La, Pr, Ho, and Tm, and to the MADDER zircon reference standard (see above) for all other trace elements. Titanite trace element data were standardized to the USGS GSE-1G geochemical reference standard and are reported in Appendix D.

Calculated Eu and Ce anomalies

The magnitude of the redox-sensitive Eu and Ce anomalies can be quantified by the expressions: $Eu/Eu^* = Eu_{CN}/[Sm_{CN}^{(1/2)}*Gd_{CN}^{(1/2)}]$ and $Ce/Ce^* = Ce_{CN}/[La_{CN}^{(2/3)}*Nd_{CN}^{(1/3)}]$ where CN refers to chondrite-normalized values (McDonough and Sun, 1995). However, the Ce anomaly is difficult to measure accurately due to large analytical uncertainties and limits of determination for low abundance La or Pr in zircon by SIMS or LA-ICP-MS methods. Instead of

This is a preprint, the final version is subject to change, of the American Mineralogist (MSA)
Cite as Authors (Year) Title. American Mineralogist, in press.
(DOI will not work until issue is live.) DOI: http://dx.doi.org/10.2138/am-2017-6053

using the Ce/Ce* calculation, we have used the Ce/Nd ratio as a proxy for the Ce anomaly following initial proposals by Olson (2015) and Lu et al. (2016).

Calculated zircon and titanite temperatures

Ti-in-zircon and Zr-in-titanite temperatures can be estimated for the melt if the activities of TiO_2 and SiO_2, and the pressure of crystallization can be estimated where $T^{Zir}(^oC) = -(4800\pm86)/[\log(Ti\ ppm) - (5.711\pm0.072) + \log(\alpha SiO_2/\alpha TiO_2)] - 273.15$ and $T^{Tit}(^oC) = [7708+960*P(GPa)]/[10.52 - \log(\alpha TiO_2/\alpha SiO_2) - \log(Zr\ ppm)] - 273.15$ (Ferry and Watson, 2007; Hayden et al., 2008). Estimates of 0.5-0.7 for αTiO_2 are generally appropriate for most volcanic arc magmas that are buffered by Ti-bearing phases (e.g., ilmenite or titanite) and an estimate of $\alpha SiO_2 = 1.0$ is appropriate for quartz-saturated igneous rocks (Watson et al., 2006; Claiborne et al., 2010; Walker et al., 2013). Underestimations of the αTiO_2 may cause a maximum decrease in Ti-in-zircon temperatures of 20º C (Watson et al., 2006; Claiborne et al., 2010), and a maximum increase in Zr-in-titanite temperatures of 20º C (Hayden et al., 2008). Errors of 0.1 GPa in the pressure estimates would cause a systematic 10-15º C shift in Zr-in-titanite temperatures at 700-800º C. The largest single contributor of uncertainty is caused by zircon and titanite sector zoning that may skew temperature calculations by ±15-20º C in zircon (Dilles et al., 2015) and up to ±50-70º C in titanite between the temperature range of 700 and 800º C (Hayden et al., 2008).

Results

Petrography and mineralogy

Major and accessory mineral phases and textures of igneous rocks in the Pebble district (Olson, 2015) are summarized in Table 1 and provide constraints for mineral-melt trace element partitioning and melt evolution for Pebble district intrusions. Most pre-mineral Late Cretaceous intrusions (99-95 Ma) are medium-grained and hypidiomorphic-granular, but volumetrically, most alkalic rocks include monzonite porphyry with phenocrysts up to 6 mm and a groundmass with a grain size <0.3 mm (Table 1). The mineralogy of the bulk of these pre-mineral intrusions is dominated by plagioclase, biotite, and augite, with accessory magnetite and apatite. The latest of these intrusions (e.g., late monzonite porphyries and granodiorite sills) have nearly subequal quantities of biotite and amphibole but lack augite, and this change reflects an increase of magmatic water content with time. Rare diamond-shaped mineral sites containing hydrothermal magnetite are found in some of the most differentiated monzonite porphyries and are inferred to be pseudomorphs of igneous titanite. Ilmenite is not observed in any of the pre-mineral Cretaceous intrusive rocks, but small amounts may have originally been present and later hydrothermally altered (Olson, 2015).

The bulk of the Kaskanak batholith is composed of granodiorite that ranges from medium-grained hypidiomorphic granular to strongly porphyritic in texture. These rocks contain abundant plagioclase and amphibole, minor K-feldspar and quartz with accessory magnetite (2-3 vol.%), biotite (<1 vol.%), and titanite (0.5-2.0 vol.%), and is interpreted to be more oxidized and hydrous than the pre-mineral intrusions based on the abundance of titanite and amphibole. Mineralized porphyry dikes are characteristically crystal-rich and contain ≥75 vol.% phenocrysts in early granodiorite porphyry and ≥50 vol.% in late quartz granite porphyry. Quartz and K-feldspar phenocrysts are absent from early granodiorite porphyry but are present up to 2 vol.% of each in late granite porphyry. Porphyritic phases of the Kaskanak batholith have a fine-grained

This is a preprint, the final version is subject to change, of the American Mineralogist (MSA)
Cite as Authors (Year) Title. American Mineralogist, in press.
(DOI will not work until issue is live.) DOI: http://dx.doi.org/10.2138/am-2017-6053

303 groundmass dominated by quartz and K-feldspar that ranges from 0.3-1 mm graphic texture in
304 "transitional" granodiorite and 0.02 to 0.3 mm aplitic texture in porphyry intrusions.
305
306 **Whole-rock geochemistry**
307 **Jurassic(?) mafic roof pendants.** Basalt and gabbro bodies occur as roof pendants of the
308 Kaskanak batholith and Koktuli Mountain pluton (Fig. 2). Locally, the basalt crosscuts and
309 includes inclusions of the gabbro. Their major and trace element compositions share similarities
310 with mafic volcanic and plutonic rocks (<55 wt.% SiO_2) of the Jurassic Talkeetna Arc in the
311 Talkeetna Mountains (Clift et al., 2005; Greene et al., 2006) and the gabbronorites of the Tonsina
312 mafic-ultramafic root of the Talkeetna arc in the Peninsular terrane (DeBari and Sleep, 1991).
313 Collectively, they are all tholeiitic, have moderate Mg #'s = 30-45), and are ilmenite-bearing.
314 The gabbro and basalt in the Pebble district are relatively enriched in Ti, Ni, Cr, and V (Fig. 5
315 and Fig. 7) compared to most other Talkeetna Arc volcanic and plutonic rocks, and thus are more
316 primitive. They are also relatively enriched in HFSEs such as Nb, Ta, Zr, and Hf (Appendix A).
317 Therefore, Pebble gabbro and basalt may be similar in composition and age to the Talkeetna Arc,
318 but are most similar to the more primitive Tosina segment. Alternatively, they could be
319 correlative with the Triassic Chilikadrotna Greenstones for which comparative geochemical data
320 are lacking (Detterman and Reed, 1980; Wallace et al., 1989; Amato et al., 2007c). Similar
321 enrichments in Ti, Ni, Cr, V, and HFSEs are observed in the mafic rocks of the Tlikakila
322 Complex near Lake Clark, but these rocks all have higher Mg #'s ranging between 50 and 75 for
323 similar compositions. They have been interpreted as primarily Late Triassic in age based on
324 Norian fossils in sedimentary units (Wallace et al., 1989; Amato et al., 2007a), but the lower
325 bounding age of plutonic rocks is inferred based on the sedimentary units, and thus it cannot be

This is a preprint, the final version is subject to change, of the American Mineralogist (MSA)
Cite as Authors (Year) Title. American Mineralogist, in press.
(DOI will not work until issue is live.) DOI: http://dx.doi.org/10.2138/am-2017-6053

ruled out that some igneous components overlap with the Talkeetna Arc. Other lines of evidence such as Sr-Nd isotopes and detrital zircons (discussed later) suggest these rocks may not be directly correlative with the gabbro and basalt found in the Pebble district. Nevertheless, the elevated Ni (ca 55-150 ppm) and Cr concentrations (ca 115-465 ppm) in the Pebble basalt and gabbro distinguish them from the most primitive Late Cretaceous and younger intrusions in the district, which are basaltic andesites (Fig. 4). The Kahiltna flysch at Pebble also contains elevated Ni (ca. 27-34 ppm) and Cr (ca. 79-96 ppm) that likely reflects the composition of primitive regional mafic and ultramafic rocks as a detrital source.

Late Cretaceous igneous rocks. Late Cretaceous intrusions include three distinctive geochemical suites: high-K calc-alkaline sills, alkaline stocks and dikes, and the late high-K calc-alkaline Kaskanak batholith. The geochemical differences distinguishing the three suites are described further below. All intrusions are magnetite-bearing, oxidized, and range in composition from metaluminous to weakly peraluminous with aluminum saturation indices (A/CNK) $\leq$ 1.1 (Fig. 5). Trace elements are characterized by Nb, Ta, and Ti depletions typical of volcanic arcs (e.g., Ryerson and Watson, 1987), and enrichments of large ion lithophile elements (LILE) and fluid-mobile elements (Sr, K, Cs, Rb, Ba, U, Th, Pb) compared to MORB (Fig. 6). The Sr/Y and La/Yb ratios of these intrusions are relatively low compared to porphyry deposit intrusions hosted by continental crust, but fall within typical ranges observed for porphyry deposit intrusions hosted by oceanic arc terranes (Fig. 7; Richards and Kerrich, 2007). The V/Sc ratios of Late Cretaceous intrusions range from 10 to 160 and, except for the mafic end-members of the alkaline suite (<55 wt.% SiO_2), are similar to or greater than the V/Sc ratios (10 to 20) typical of porphyry deposit magmas (Fig. 7; Loucks, 2014). The V/Sc ratio increases gradually with increasing silica, which has been proposed by Loucks (2014) to reflect strongly oxidized

This is a preprint, the final version is subject to change, of the American Mineralogist (MSA)
Cite as Authors (Year) Title. American Mineralogist, in press.
(DOI will not work until issue is live.) DOI: http://dx.doi.org/10.2138/am-2017-6053

magmatic conditions where significant vanadium occurs in oxidized V^{4+} and V^{5+} valences and behaves incompatibly in the melt. Most of the elevated V compositions are likely magmatic features, but a few samples have exceptionally elevated V concentrations up to 1,600 ppm, likely as a result of hydrothermal enrichment (circled in Fig. 7). Hydrothermal enrichment of V in porphyry deposits has been proposed to preferentially occur in highly oxidized systems and where there has been considerable telescoping of the epithermal and porphyry hydrothermal footprints (Richards, 1995; Loucks, 2014).

The calc-alkaline diorite and granodiorite sills are the oldest and youngest pre-mineral intrusions in the district, respectively, and are temporally associated with alkalic intrusions (Lang et al., 2013; Olson, 2015). The diorite and granodiorite sills have many similar trace element contents suggesting common origin that includes elevated Ti, Y, Yb, and P compared to other local Cretaceous and Tertiary rocks (Figs. 5 and 6). The diorite sills have much higher V, Sc, and Ni contents, a larger negative Eu anomaly, lower HFSE (Nb, Ta, Zr, Hf) and lower LREE (La, Ce) compared to the granodiorite sills (Figs. 5, 6, 7). A single porphyritic andesite intrusion immediately west of the Pebble deposit closely shares trace element characteristics with the granodiorite sills and may be genetically related, but it differs from other rare occurrences of porphyritic andesite dikes sampled on the flanks of the Kaskanak batholith. Collectively, the geochemical differences among the pre-mineral calc-alkaline intrusive rocks may result from both greater differentiation and minor assimilation of the Kahiltna flysch or mafic basement rocks.

The lithologically diverse alkalic suite includes monzodiorite and monzonite ranging from 50 to 67 wt.% SiO_2, and pyroxenite with 42 wt.% SiO_2. The HFSE and REE concentrations of the alkaline suite are mostly lower than the calc-alkaline sills and similar to the Kaskanak

372 granodiorite (Figs. 6 and 8). Early monzodiorite stocks are spatially associated with biotite
373 pyroxenite bodies interpreted as cogenetic cumulates. The biotite pyroxenite cumulates have
374 similar middle rare earth element (MREE) slopes and abundances to other alkalic intrusions, but
375 they are relatively depleted in both light and heavy rare earth elements consistent with
376 accumulation of MREE-enriched clinopyroxene. The biotite pyroxenite cumulates have
377 concentrations of Ti, Ni, and Cr similar to other alkalic rocks which are much lower than the
378 concentrations observed in the basalt and gabbro roof pendants. Rare shoshonite dikes also occur
379 and have similar compositions to the monzodiorite stocks (Fig. 4), but they contain accumulated
380 magnetite (up to 5 to 7 vol.%) and abundant rafts of plagioclase and clinopyroxene (Table 1).
381 They also have large positive whole-rock Eu anomalies indicating they may have assimilated
382 plagioclase-rich rocks and/or accumulated plagioclase. Early to late monzonite porphyry dikes
383 crosscut the biotite pyroxenite cumulate rocks, and some late monzonite porphyry dikes locally
384 crosscut associated magmatic-hydrothermal diatreme breccias. Some late monzonite porphyries
385 contain rare titanite (Table 1) and have whole-rock Eu anomalies that change from small
386 negative anomalies to positive anomalies with magmatic differentiation. This change is also
387 observed during differentiation from Kaskanak granodiorite to the most evolved granite
388 porphyry (Fig. 8).

389 The bulk of the Kaskanak batholith is calc-alkaline granodiorite in composition with
390 volumetrically minor amounts of porphyritic andesite dikes and a series of more differentiated
391 granodiorite to granite porphyry dikes (Olson, 2015). The porphyritic andesite dikes and
392 granodiorite of the Kaskanak batholith have 56 to 67 wt.% SiO_2 and overlap in major and trace
393 element compositions with alkalic suite having the same SiO_2 contents. Many of the porphyritic
394 andesite dikes occur along the flanks of the Kaskanak batholith and have been weakly affected

This is a preprint, the final version is subject to change, of the American Mineralogist (MSA)
Cite as Authors (Year) Title. American Mineralogist, in press.
(DOI will not work until issue is live.) DOI: http://dx.doi.org/10.2138/am-2017-6053

by sodic-calcic alteration resulting in reduced alkalis and LILE (Fig. 6). A sample of porphyritic andesite in the 1 Gold Zone contains the lowest SiO_2 and was chosen as a potential parental magma for purposes of modeling the Kaskanak batholith magmatic evolution (discussed later). The more silicic and younger Kaskanak granodiorite and granite porphyry dikes (67 to 77 wt.% SiO_2) lie along the same trends in variation and spider diagrams, but are evolved to lower transition metal (Mg, Fe, Cr, Sc), HFSE, and REE concentrations (Figs. 6, 7 and 8). The most differentiated granite porphyry dikes are REE-poor, have a pronounced concave upward chondrite-normalized REE profile, and have a range from no Eu anomaly to a moderate positive Eu anomaly in the most silicic compositions (Fig. 8). For all the Kaskanak batholith intrusions, Sr/Y ratios range from 20 to 65 (from volcanic arc to adakitic composition) and La/Yb ratios range from 4 to 16 (normal volcanic arc) with the highly evolved porphyries having the highest ratios; note that Sr has been significantly depleted in many hydrothermally altered samples, which are excluded from the reported Sr/Y ratios (Fig. 7). The V concentrations and V/Sc ratios of samples of the Kaskanak batholith are also highly elevated especially in the most evolved samples. The V/Sc ratios are much higher than typical porphyry copper magmas reported by Loucks (2014). Furthermore, the most leucocratic granite porphyries are highly enriched in some incompatible LILEs such as U, Th and Rb, and strongly depleted in Ti compared to less evolved granodiorite and quartz granite porphyry intrusions (Figs. 5 and 6). The highly elevated LILEs in these leucocratic granites may be a product of late-stage filter-pressing or late-stage crystallization of segregated pockets of melt near the solidus.

Paleocene – Eocene igneous rocks. Igneous rocks associated with the Talarik Formation, and the Koktuli Volcanics and associated plutonic rocks are metaluminous, calc-alkaline rocks with SiO_2 concentrations that range from 53-76 wt.% SiO_2. These rocks have

This is a preprint, the final version is subject to change, of the American Mineralogist (MSA)
Cite as Authors (Year) Title. American Mineralogist, in press.
(DOI will not work until issue is live.) DOI: http://dx.doi.org/10.2138/am-2017-6053

418 depletions in Nb, Ta, and Ti concentrations similar to Late Cretaceous igneous rocks. They have
419 elevated concentrations of Th, U, and REE relative to most Late Cretaceous intrusions (Fig. 5).
420 The Mg, Sc, Ni and Cr concentrations in the basaltic andesites are also relatively depleted
421 compared to the gabbro and basalt roof pendants. Phenocryst-poor Paleocene dacite dikes that
422 crosscut mineralization in the East Zone are strongly depleted in MREEs and have elevated Sr/Y
423 and La/Yb ratios similar to some of the most differentiated Late Cretaceous intrusions including
424 monzonite porphyry and leucocratic granite porphyry dikes (Fig. 7). The V/Sc ratios for all
425 Paleocene and Eocene igneous rocks generally are less than 10 and fall outside the field of most
426 porphyry deposit intrusions (Fig. 7).
427
428 **Radiogenic isotopes**
429 The Sr and Nd isotopic data from this study include 1 sample from a gabbro roof
430 pendant, 10 samples from Late Cretaceous intrusions, and 1 sample from a Paleocene andesite
431 dike (Table 2). Initial $^{87}Sr/^{86}Sr$ and $^{143}Nd/^{144}Nd$ ratios were calculated at 180 Ma, 90 Ma, and 65
432 Ma, respectively, and are compared to other Sr and Nd isotopic data for Late Cretaceous and
433 Paleocene igneous rocks from the Pebble deposit (Fig. 9; Ayuso et al., 2013; Goldfarb et al.,
434 2013). Initial $^{87}Sr/^{86}Sr$ and $^{143}Nd/^{144}Nd$ isotopic compositions of all rocks from this study have a
435 range of 0.70329 – 0.70424 and 0.51270 – 0.51284 (εNd_i = +4.4 – +6.1), respectively, and where
436 other data are included, the total range is 0.70329 – 0.70554 and 0.51257 – 0.51287 (εNd_i = +1.0
437 – +6.3), respectively.
438 The data are broadly comparable, however, Ayuso et al. (2013) reported εNd_i values for
439 Cretaceous rocks (εNd_i = +1.0 – +4.5) that are mostly lower than the εNd_i values from Goldfarb
440 et al. (2013) and this study combined (n = 20, εNd_i = +4.4 – +6.3). Photos of several samples of

This is a preprint, the final version is subject to change, of the American Mineralogist (MSA)
Cite as Authors (Year) Title. American Mineralogist, in press.
(DOI will not work until issue is live.) DOI: http://dx.doi.org/10.2138/am-2017-6053

441 drill core analyzed by Ayuso et al. (2013) contain xenoliths of the Kahiltna flysch (εNd_i = -1 – -
442 5; Aleinikoff et al., 2000). Inclusion of the Kahiltna flysch clasts in analyzed samples or local
443 melting of the Kahiltna flysch by Pebble intrusions would both result in anomalously low εNd_i
444 values such as those reported by Ayuso et al. (2013).
445 Subdividing the total dataset of igneous rocks at Pebble into Jurassic, Cretaceous, and
446 Paleocene/Eocene subsets ($^{87}Sr/^{86}Sr_i$ ratios = 0.70338, 0.70329 – 0.70467, 0.70348 – 0.70354,
447 respectively; $^{143}Nd/^{144}Nd_i$ ratios = 0.51270, 0.51257 – 0.51284, 0.51274 – 0.51287, respectively;
448 and εNd_i values = 5.7, 1.0 – 6.3, 3.7 – 6.2, respectively), the least radiogenic isotopic
449 compositions all overlap suggesting little change of the isotopic composition of melts from the
450 source region with time. The isotopic spread towards more radiogenic values is apparently from
451 variable amounts of assimilation of the Kahiltna flysch, the only radiogenic source identified in
452 the region.
453
454 **Trace element concentrations in zircon and titanite**
455 Zircons that grow from arc magmas have very low LREE and strongly elevated HREE
456 concentrations with distinctive positive Ce and negative Eu anomalies (Figs. 10 and 11). Zircons
457 that grow from mineralized intrusions are typically characterized by larger positive Ce anomalies
458 and smaller negative Eu anomalies than barren intrusions, which reflect the elevated magmatic
459 oxidation states (ΔNNO+1 to +3) in the mineralizing intrusions (Ballard et al., 2002; Dilles et al.,
460 2015). Additionally, small Eu anomalies may be accentuated by the suppression of plagioclase
461 crystallization in hydrous melts (Ballard et al., 2002; Hoskin and Schaltegger, 2003; Trail et al.,
462 2011; Dilles et al., 2015). Extensive amphibole, pyroxene, or minor titanite fractionation may

This is a preprint, the final version is subject to change, of the American Mineralogist (MSA)
Cite as Authors (Year) Title. American Mineralogist, in press.
(DOI will not work until issue is live.) DOI: http://dx.doi.org/10.2138/am-2017-6053

463 also increase the Yb/Gd ratio of the melt (Kay and Mpodozis, 2001; Richards and Kerrich, 2007)
464 and thus increase the Yb/Gd ratio of late crystallizing zircon.

465 Zircons trace elements from intrusions in the Pebble district are plotted in Figure 10.
466 Zircons from the diorite sills and Koktuli Mountain granodiorite have very low Eu/Eu* values
467 (mostly ≤0.3), low Ce/Nd ratios (≤22), and low Yb/Gd ratios (≤18) suggesting significant
468 plagioclase-dominated fractionation, and are the least prospective in terms of porphyry copper
469 fertility. Zircons from the alkalic monzonite porphyry appear to be spread towards lower
470 temperatures with lower recorded concentrations of Hf and elevated Ce/Nd ratios. A possible
471 contaminant could be the calc-alkaline granodiorite sills, but no definitive field evidence has
472 documented magma mingling of these intrusions. The granodiorite sills, like the Kaskanak
473 batholith, have lower temperature zircons, elevated Yb/Gd ratios (26-54), very high Eu/Eu*
474 anomalies (0.7-1.1), and very high Ce/Nd ratios (up to 126), and thus have a very fertile zircon
475 trace element signature. No known mineralization is associated with the granodiorite sills, which
476 may be a result of volatile loss coeval with the formation of large diatreme breccias (Figs. 2 and
477 3). Other barren Paleocene andesite and dacite dikes also have perspective Eu anomalies (0.6-
478 1.0), but have moderate Ce/Nd ratios (7-53) and lower Yb/Gd ratios (16-33). All intrusions of the
479 mineralized Kaskanak batholith have fertile zircon trace element signatures with high Eu/Eu*
480 values (0.4-1.1), high Ce/Nd ratios (up to 152), and elevated Yb/Gd ratios (13-56) owing to
481 extensive fractionation of amphibole and titanite under hydrous and oxidized magmatic
482 conditions.

483 Titanite in the Pebble district is present in all phases of the Kaskanak batholith and occurs
484 sparsely in some of the unaltered samples of monzonite porphyries of the alkalic suite. Outside
485 the hydrothermal footprint, the Kaskanak granodiorite contains abundant titanite (0.5-2.0 vol.%)

This is a preprint, the final version is subject to change, of the American Mineralogist (MSA)
Cite as Authors (Year) Title. American Mineralogist, in press.
(DOI will not work until issue is live.) DOI: http://dx.doi.org/10.2138/am-2017-6053

and ubiquitous, but minor zircon (<0.05 vol.%). Titanite contains high concentrations of REE and HFSE (Y, Zr, Hf, Nb, Ta, Th, and U), and titanite analyzed from the Kaskanak granodiorite contains >100 times more REE and 10-100 times more HFSE than whole-rock compositions (Fig. 11g, Appendix D). Because of the abundance of titanite and its high concentrations of HFSE and REE, mass balance dictates that the vast majority of the whole-rock HFSE and REE content resides in titanite.

The REE and HSFE contents of unaltered titanites are normally zoned and decrease from core to rim sympathetic with Y decrease from 6000 to 2000 ppm (Fig. 12). Generally, titanite chondrite-normalized REE patterns range from convex "seagull-shaped" to concave "U-shaped" profiles (e.g., $Dy_{CN}/Yb_{CN} < 1$; Fig. 11c and 12f). This observed preferential depletion of middle REE relative to light and heavy REE is due to the larger partition coefficients for the middle REE compared to light and heavy REE (Table 3; Bachmann et al., 2005; Colombini et al., 2011). At low Y contents of 300 to 2000 ppm, the REE and HFSE content and Zr-in-titanite temperature vary broadly (Fig. 12), as described above, and are not well-correlated with Y content. For example, Nb and Th strongly decrease sympathetic with the decrease of Y from early titanite cores to rims presumably as a result of titanite removing these elements from the melt, but increase sharply in some late cores and rims. These late cores and rims have relatively high Nb, Th, Nb/Ta, and Zr-in-titanite temperatures (Fig. 12). Some of these analyses correspond with observed titanite resorption features and rim overgrowths (Fig. 11a).

Ti-in-zircon and Zr-in-titanite temperatures

Ti-in-zircon and Zr-in-titanite temperatures of Late Cretaceous rocks are calculated and plotted in Figures 10b and 12a. The calculations assume activities of TiO_2 and SiO_2 of 0.7 and

1.0, respectively; and titanite crystallization pressure of 0.2 GPa for the Kaskanak batholith (see Methods for further details). The results of Ti-in-zircon temperature estimates for Late Cretaceous pre-mineral diorite sills, monzonite porphyries, and granodiorite sills are all relatively hot (930-730º C; Fig. 10b). For the younger Kaskanak batholith intrusions, Ti-in-zircon and Zr-in-titanite temperature estimates are in agreement (Figs. 10b and 12a) and suggest zircon and titanite crystallized together at lower magmatic temperatures (760-680º C). Some titanite cores and many titanite rim analyses, however, reflect higher temperatures (up to 800º C) at relatively low Y and REE concentrations (Fig. 12) and record anomalous trace element compositional variance, reflecting complicated late-stage magmatic processes correlated with fluctuations in temperature.

Trace elements of inherited zircons

Inherited zircons are relatively abundant in Late Cretaceous intrusions in the district, especially in the early monzonite porphyries of the alkalic suite (commonly >95% inheritance) and the diorite and granodiorite sills (commonly >50% inheritance). The histograms of inherited zircons indicate that Cretaceous ages dominate with progressively fewer Jurassic and Triassic ages, and 12% Paleozoic ages as old as Cambrian (Fig. 13b). All inherited zircons exhibit normal oscillatory zoning textures, elevated Th/U ratios (e.g., ≥0.4), and REE abundances consistent with an original igneous source. The maximum values of Eu/Eu*, Yb/Gd, and Ce/Nd occur <200 Ma during the Jurassic – Cretaceous periods (Fig. 13c-e). In contrast, the most reduced values occur in the Permian to Triassic periods from ~300 to 200 Ma (Fig. 13d-e) consistent with timing of late Skolai arc magmatism (~290-320 Ma; Fig. 1) and the Nikolai greenstone flood basalts (~240-250 Ma) within the Wrangellia terrane (Beard and Barker, 1989). Pennsylvanian to

This is a preprint, the final version is subject to change, of the American Mineralogist (MSA)
Cite as Authors (Year) Title. American Mineralogist, in press.
(DOI will not work until issue is live.) DOI: http://dx.doi.org/10.2138/am-2017-6053

Cambrian inheritance has slightly larger Eu/Eu* and Ce/Nd values, and much larger Yb/Gd ratios. Apart from the Skolai arc intrusions, the sources for many of these older zircons are unknown, and their trace element composition suggests derivation from more oxidized and fractionated melts than the Permian to Triassic zircons.

Discussion

The geochemical composition of Late Cretaceous magmatic arc rocks that developed after suturing of the WCT to the North American continental margin in the Iliamna region is more evolved than the older pre- to syn-collisional Jurassic Talkeetna Arc basement rocks. Late Cretaceous to Eocene intrusive rocks are alkaline to high-K calc-alkaline with elevated LILEs and HFSEs compared to the Talkeetna Arc magmatic rocks that range from tholeiitic to calc-alkaline compositions (Greene et al., 2006). Late Cretaceous intrusions have a larger range of La/Yb and Sr/Y ratios (La/Yb = 5-18; Sr/Y= 20-55) compared to the Talkeetna Arc volcanic rocks (La/Yb = 2-5; Sr/Y=3-30; Clift et al., 2005). Sr/Y ratios of Late Cretaceous intrusions overlap the adakite field (Fig. 7a), but Late Cretaceous and Jurassic magmatic rocks both lack adakite-like La/Yb ratios > 20 (Fig. 7b; Richards and Kerrich, 2007). Late Cretaceous to Eocene igneous rocks also have large arc-like depletions in Nb, Ta, and Ti compared to the Talkeetna Arc volcanic rocks. These depletions become more pronounced with arc maturation consistent with the findings of Amato et al. (2007b). In sharp contrast, Pebble gabbro and basalt roof pendants, inferred to be Jurassic in age, lack these depletions. Chondrite-normalized REE profiles and low La/Yb ratios of all regional intrusions are consistent with volcanic arc magmatism developed in a relatively thin crust where heavy REE-rich garnet was not stable. Residual garnet or garnet fractionation would significantly increase the observed La/Yb and Sr/Y

ratios if present (Kay and Mpodozis, 2001). The crustal thickness during Cretaceous to Eocene magmatism is unknown, but likely is similar or less than the modern crustal thickness estimate of 30 km for the Iliamna Quadrangle based on gravity surveys (Barnes, 1977) and therefore crustal garnet would be unlikely. The most primitive Late Cretaceous igneous rocks exposed in the region are shoshonite to andesite in composition (Fig. 4), similar to other arc suites developed in thin crust. These rocks likely originated via hybridization of mantle-derived and lower crustal melts (Hildreth and Moorbath, 1988; Annen et al., 2006). The most mafic Paleocene and Eocene magmatic rocks share a similar range from differentiated basaltic andesite to andesite, but are locally all calc-alkaline in composition. In contrast, mafic end members of the Jurassic Talkeetna Arc commonly contain more abundant primitive basalts, gabbros, and gabbronorites (Detterman and Reed, 1980; DeBari and Sleep, 1991; Nokleberg et al., 1994; Clift et al., 2005; Greene et al., 2006). Nonetheless, the primitive Talkeetna arc magmas were contaminated by some older crustal components on the basis of slightly radiogenic initial Sr and Nd isotopes (Fig. 9), and inherited Paleozoic zircons in both the West Talkeetna Mountains and the Alaska Peninsula (Clift et al., 2005; Greene et al., 2006; Rioux et al., 2007; 2010). In comparison, the Pebble Late Cretaceous intrusions may have also assimilated older Paleozoic crust from the roots of the Peninsular terrane, but also variably assimilated the Late Jurassic-Early Cretaceous Kahiltna flysch and possibly some Jurassic arc basement rocks on basis of inherited zircons and Sr and Nd isotopes.

Source region and crustal assimilation

The magnitude of crustal assimilation by Late Cretaceous intrusions is difficult to constrain without context for possible sources. Inherited (xenocrystic) zircons provide a robust

This is a preprint, the final version is subject to change, of the American Mineralogist (MSA)
Cite as Authors (Year) Title. American Mineralogist, in press.
(DOI will not work until issue is live.) DOI: http://dx.doi.org/10.2138/am-2017-6053

line of evidence for crustal assimilation and provide evidence for the age of unexposed basement rocks in the region. Most of the inherited zircons in Late Cretaceous intrusions in the Pebble district are likely sourced from the Kahiltna flysch. However, some monzonite porphyry intrusions contain predominantly Early Devonian – Pennsylvanian xenocrystic zircons that suggest contributions from basement rocks. The lack of inherited Proterozoic zircons rules out contributions from the Intermontane superterrane and restricts inherited zircons to a WCT origin. Nonetheless, anomalous Proterozoic and few Archean zircons have been found east of Lake Clark in detritus associated with the Tlikakila Complex (Amato et al., 2007a) and within xenoliths in Mount Redoubt volcanic rocks (Bacon et al., 2012). Possible sources of recycled Paleozoic zircons within the Peninsular terrane in SW Alaska include Paleozoic pelitic and quartz-mica schists, which are discontinuously exposed as roof pendants in Triassic and younger plutons between the southern margins of the Western Alaska Range (Csejtey et al., 1978; Nokleberg et al., 1994; Amato et al., 2007c) and north side of the Border Ranges fault system (Nokleberg et al., 1994). Some Pennsylvanian to Early Permian zircons may be derived from Skolai Arc plutons (Aleinikoff et al., 1988; Gardener et al., 1988; Beard and Barker, 1989) that are exposed to the east in the Wrangellia and Alexander terranes of the Talkeetna and East Alaska ranges (Fig. 1). Nonetheless, Skolai Arc plutons may form basement that underlies the Kahiltna flysch in the SW Alaska Range as indicated by Pennsylvanian gabbroic xenoliths in volcanic rocks from Mt. Redoubt (Fig. 1; Bacon et al., 2012). Inherited Paleozoic zircons are also reported from Jurassic plutonic rocks along the Alaska Peninsula (Amato et al., 2007a), volcanic tuffs of the Kamishak and Talkeetna Formations (Pálfy et al., 1999), and in some Jurassic plutons in the Western Talkeetna Mountains (Rioux et al., 2007).

This is a preprint, the final version is subject to change, of the American Mineralogist (MSA)
Cite as Authors (Year) Title. American Mineralogist, in press.
(DOI will not work until issue is live.) DOI: http://dx.doi.org/10.2138/am-2017-6053

Sr and Nd isotopic ratios are generally primitive and restricted in range for melts throughout the WCT due to its youth and overall primitive composition relative to average continental crust. Nonetheless, some Jurassic and older basement rocks have slightly elevated Sr isotopic ratios exhibiting initial $^{87}Sr/^{86}Sr > 0.7050$ (Fig. 9) that are likely caused by metasomatic alteration by connate fluids during greenschist facies metamorphism in the WCT (Detterman and Reed, 1980; Nokleberg et al., 1994; Wallace et al., 1989: Amato et al., 2007a). In contrast, initial $^{87}Sr/^{86}Sr$ ratio ranges of 0.70329 to 0.70452 and initial $^{143}Nd/^{144}Nd$ ratio ranges of 0.51257 to 0.51284 are primitive and very restricted in Late Cretaceous and younger intrusions which are not metamorphosed in the Pebble district (Fig. 9). The Nd isotopic compositions ($\varepsilon Nd_i = +4.6 – +6.3$) of any of the intrusions in the district, including those of the Talkeetna Arc, are not likely affected by external hydrothermal fluids because Nd is an immobile element, and thus a more robust tracer of radiogenic contamination. The Nd isotopic data from these intrusions overlap with those of the Talkeetna Arc volcanics in the West Talkeetna Mountains and along the Alaska Peninsula (Fig. 9; Rioux et al., 2007; 2010). In the Pebble district, the Sr and Nd isotopic compositions are similar for the Kaskanak granodiorite and the gabbro roof pendants interpreted as Jurassic in age (Fig. 9c). In contrast, older Triassic gabbros of the Tlikakila Complex located 100 km to the northwest (Wallace et al., 1989; Amato et al., 2007a) have quite variable Nd isotopic compositions ($\varepsilon Nd_{215} = -1.2 – +9.3$), likely due to crustal contamination by an unknown radiogenic source, which are consistent with the observations of inherited Proterozoic and Archean zircons and the inferred metasomatic alteration by connate fluids noted above. Because inherited Proterozoic zircons are rare in Talkeetna Arc magmatic rocks (Pálfy et al., 1999; Amato et al., 2007c) and are absent from all of the Late Cretaceous to Eocene intrusions in the

This is a preprint, the final version is subject to change, of the American Mineralogist (MSA)
Cite as Authors (Year) Title. American Mineralogist, in press.
(DOI will not work until issue is live.) DOI: http://dx.doi.org/10.2138/am-2017-6053

Pebble district, it is inferred that very little, if any, ancient continental crust exits beneath the Pebble district.

The primary contamination difference between the Jurassic and older basement rocks and the Late Cretaceous to Eocene igneous rocks is that the latter was contaminated by the Late Jurassic – Early Cretaceous Kahiltna flysch, the principal exposed country rock to the intrusions. Note that the Kahiltna flysch is more radiogenic than the Talkeetna Arc and the Tlikakila Complex which are representative of the basement rocks from which the flysch is partially derived (Fig. 9). To constrain the amount of assimilation of the Kahiltna flysch required for Late Cretaceous and Paleocene intrusions, two-component mixing models (Faure, 1998) were calculated between three selected igneous samples and an average composition of the Kahiltna flysch with isotopic compositions recalculated to both 90 m.y. and 65 m.y. ago to reflect the age of the mixing (Fig. 9; Appendix E). Note that the Kahiltna flysch isotopic composition at 65 Ma would be slightly more radiogenic than at 90 Ma or 125 Ma (Fig. 9a). The Sr isotopic data utilized for the Kahiltna flysch from Aleinikoff et al. (2000) ($^{87}Sr/^{86}Sr_{125\ m.y.}$ = 0.70549 – 0.70715) overlaps with a single Sr isotopic analysis of the flysch locally at Pebble ($^{87}Sr/^{86}Sr_{125\ m.y.}$ = 0.70554, Ayuso et al., 2013) and is therefore approximately representative. The three igneous end members in the models include: a) Kaskanak granodiorite, b) a diorite sill, and c) a Paleocene monzonite porphyry dike (see Appendix E for trace element and isotopic compositions). The least radiogenic Late Cretaceous or Paleocene sample composition recorded in the district ($^{87}Sr/^{86}Sr_i$ = 0.70330, $^{143}Nd/^{144}Nd_i$ = 0.512844, εNd_i = +6.3) is assumed to represent the minimum isotopic enrichment for homogenized parental melts supplied from the lower crust for the region and was utilized as the starting isotopic composition for the igneous rocks in the mixing models. The curvature of the mixing models (Fig. 9b) reflects the whole-rock

This is a preprint, the final version is subject to change, of the American Mineralogist (MSA)
Cite as Authors (Year) Title. American Mineralogist, in press.
(DOI will not work until issue is live.) DOI: http://dx.doi.org/10.2138/am-2017-6053

Sr and Nd composition of the igneous samples relative to the composition in the Kahiltna flysch (i.e., the susceptibility of the intrusions to be isotopically contaminated by the Kahiltna flysch). The εNd_i versus 1/Nd plot (Fig. 9c) suggests that maximum assimilation of the Kahiltna flysch by Late Cretaceous or Paleocene intrusions was predominantly minor (<20 wt.%), except in the case of some narrow monzonite dikes or granodiorite sills that likely have assimilated up to 50 wt.% locally. If a more radiogenic composition for the Kahiltna flysch is utilized (Fig. 9a), as might be the case for flysch stratigraphically high in the Kahiltna basin or closer to the suture zone with the Intermontane superterrane to the north, then the mixing-models would require a smaller percentage of assimilation of the flysch. Based on these models, the Kaskanak granodiorite is one of the least-radiogenic samples in the district (see Fig. 9c) and likely assimilated very little Kahiltna flysch (≤10 wt.%). Therefore, minor assimilation of the Kahiltna flysch likely had little effect on the fertility of Late Cretaceous melts.

Oxidation recorded by zircons

Among the REEs, only $Ce^{(3+, 4+)}$ and $Eu^{(2+, 3+)}$ occur in multiple valence states under natural magmatic conditions and thus may be used to monitor relative changes in the oxidation state of the melt. They are particularly useful in highly oxidized magmatic systems where other monitors (e.g., Fe-Ti oxides) are not applicable. Progressive oxidation during magmatic evolution and cooling has been documented in several porphyry environments (Ballard et al., 2002; Dilles et al., 2015). Chondrite-normalized Eu/Eu* and Ce/Nd, a proxy for chondrite-normalized Ce/Ce*, are used here to monitor the relative oxygen state of the melt upon late-stage zircon saturation (Olson, 2015; Lu et al., 2016). Eu/Eu* values ≥0.4 are typical of most porphyry Cu deposits and reflect oxidized and hydrous arc magmas (Ballard et al., 2002; Dilles et al.,

2015). Ce/Nd (and Ce/Ce*) ratios are also generally elevated and reflect oxidized conditions of mineralized porphyry intrusions, but overlap with data from barren intrusions and thus are not as effective as Eu/Eu* for discriminating melt fertility. For example, Ce/Nd ratios of zircons from mineralized porphyries in the Chuquicamata district range from 0 to 77 compared to barren, older intrusions of the Montecristo Intrusive Complex which have a range of 2 to 12 (Ballard et al., 2002). However, these mineralized porphyries contrast sharply with the range of zircon Ce/Nd ratios from mineralized intrusions in the neighboring Los Picos-Fortuna district of similar age. In the Los Picos-Fortuna district, mineralized porphyry intrusions have zircon Ce/Nd ratios ≤ 7 and pre-mineral barren intrusions completely overlap having ratios ranging from 2 to 10 (Ballard et al., 2002). Lu et al. (2016) also reported overlapping Ce/Nd ratios for zircon that range from 3 to 100 for intrusions genetically associated with porphyry Cu±Mo±Au deposits and 0 to 40 from unrelated barren magmatic suites. We interpret the reported large range of Ce/Nd ratios in zircons from both barren and mineralized intrusions to reflect complications of varying oxidation states of melts in equilibrium with zircon and the presence of fractionating accessory minerals that sequester the REE^{3+} during late-stage differentiation and zircon crystallization (cf., Grimes et al., 2015). Titanite or apatite fractionation, for example, may modify the Ce anomaly by suppressing REE^{3+} from the melt.

In the Pebble district, nearly all mineralized intrusions of the Kaskanak batholith have zircon Eu/Eu* ratios > 0.4 (Fig. 10). Pre-mineral Cretaceous and post-mineral Paleocene intrusions in the district have similar zircon Eu/Eu* values that suggests they also were hydrous and oxidized arc magmas. However, there is a clear distinction with regards to the diorite sills and the granodiorite of Koktuli Mountain that show consistently low Eu/Eu* values, indicating that they were likely both less-oxidized and less-hydrous relative to the mineralized intrusions.

This is a preprint, the final version is subject to change, of the American Mineralogist (MSA)
Cite as Authors (Year) Title. American Mineralogist, in press.
(DOI will not work until issue is live.) DOI: http://dx.doi.org/10.2138/am-2017-6053

Zircon Ce/Nd ratios of mineralized intrusions range from 7 to 152 and mostly overlap with the pre-mineral Cretaceous intrusions that range from 4 to 126. Non-mineralized Paleocene intrusions have a smaller range of zircon Ce/Nd ratios that range from 7 to 53 and the Eocene Koktuli Mountain granodiorite in comparison is more restricted in range (Ce/Nd = 10 to 22).

Effects of titanite crystallization

Titanite, a common accessory mineral in relatively oxidized plutonic rocks, generally has a crystallization temperature of <780°C (Dilles, 1987; Wones, 1989; Piccoli et al., 2000; Mazdab and Wooden, 2007; Mazdab et al., 2008) and occurs in many crystal-rich volcanic rocks (e.g., Fish Canyon Tuff, Bachmann and Bergantz, 2008). In the Kaskanak batholith, titanite is the most abundant accessory mineral phase and the major sink for HFSEs and REEs. Magmatic titanite strongly incorporates all REEs, particularly the MREEs, with partition coefficients at low magmatic temperatures of 700-800°C that range between 100-1000 (Bachmann et al., 2005; Colombini et al., 2011). Unlike early crystallization or fractionation of amphibole or pyroxene, minor crystallization or fractionation of titanite can extremely depress the REE content of the melt and the relative proportions of each REE, and therefore readily effects geochemical proxies such as Sr/Y and La/Yb ratios (Bachmann et al., 2005; Richards and Kerrich, 2007; Glazner et al., 2008; Colombini et al., 2011). During solidification of Kaskanak granodiorite, late-stage titanite fractionation reduces the HFSE and REE of remaining melt and together with other crystallizing minerals is responsible for differentiation to produce the most evolved and silicic granodiorite to granite porphyry dikes that are HFSE- and REE-poor (Figs. 6 and 8).

Crystal fractionation modeling of the Kaskanak batholith

This is a preprint, the final version is subject to change, of the American Mineralogist (MSA)
Cite as Authors (Year) Title. American Mineralogist, in press.
(DOI will not work until issue is live.) DOI: http://dx.doi.org/10.2138/am-2017-6053

714 Simple Rayleigh fractionation models are used here to assess lower-crustal and late-stage
715 upper-crustal differentiation of the Kaskanak batholith. The most primitive Late Cretaceous rock
716 compositions observed in the district include small volumes of shoshonite and porphyritic
717 andesite dikes, the latter which are spatially and temporally associated with the Kaskanak
718 batholith (Olson, 2015). These porphyritic andesite dikes represent a very small proportion
719 (<1%) of the exposed Kaskanak batholith, suggesting most magmatic differentiation and
720 maturation occurred in the deep or middle crust from which magma batches periodically
721 rejuvenated the intermediate to felsic crystal mushes in the shallow crust.
722 **Model a – differentiation of andesite parental melts.** Rayleigh fractionation modeling
723 of a parental andesite composition to produce the Kaskanak granodiorite was undertaken for a
724 series of trace elements (model a; Table 3). A best fit ($\sum(R^2) = 5.5$, excluding Sr) was obtained
725 by minimizing the residuals of most selected trace elements within 0 – 10% of the observed
726 daughter melt composition (Table 4). The model is largely constrained by observed mineral
727 phases and Sc, Y, Nb, P_2O_5, and REE, but the model fails to adequately describe Sr, which is
728 readily affected by hydrothermal alteration (Fig. 14a). Model (a) also invokes up to 0.18 wt.%
729 allanite in the bulk cumulus that is required to reduce the LREE, whereas apatite, another LREE-
730 bearing phase, is restricted by phosphorus (Fig. 14e). Allanite is rarely observed in these rocks
731 (Olson, 2015), possibly due to hydrothermal alteration to epidote. According to the model,
732 approximately 10-14 wt.% crystal fractionation of a hornblende diorite bulk cumulus with 54.5
733 wt.% amphibole, 32.5 wt.% plagioclase, 7.7 wt.% magnetite, and 5.1 wt.% apatite, and 0.18
734 wt.% allanite could produce the observed range of granodiorite compositions (Fig. 14). Note that
735 amphibole fractionation produces a minor depression of REE contents when the rhyolitic
736 partition coefficients from Mount Mazama, Oregon, are applied (Bacon and Druitt, 1998; model

This is a preprint, the final version is subject to change, of the American Mineralogist (MSA)
Cite as Authors (Year) Title. American Mineralogist, in press.
(DOI will not work until issue is live.) DOI: http://dx.doi.org/10.2138/am-2017-6053

a in Fig. 14f). The progressively greater depletions of Nb and REE are observed in the evolution sequence from the Kaskanak granodiorite to granite porphyry, which have an order of magnitude reduction in REE contents. Such depletions cannot be obtained by fractionation of any assemblage of high temperature crystallizing minerals, such as model a, and rather require fractionation of Nb- and REE-enriched titanite.

Estimating Nb and REE partition coefficients for titanite. In order to model the effect of titanite-fractionation on melt, we necessarily constrained the partition coefficients for titanite in the Kaskanak granodiorite (Table 3). In general, titanite partition coefficients (Kd) are poorly constrained for intermediate-felsic, metaluminous, low-temperature (e.g., 700-800° C) calc-alkaline magmas, and published results for such compositions are highly variable and few in number (e.g., Bachmann et al., 2005; Colombini et al., 2011). We estimated titanite partition coefficients for the Kaskanak granodiorite from measured titanite$_{max}$/whole-rock$_{max}$ concentrations utilizing only high-Y (>2,000 ppm) titanite core analyses because the early high-Y titanite crystallized from a melt whose trace element content was initially most similar to whole-rock (Table 3). These high-Y titanite cores are apparently unaffected by complicated late-stage magmatic processes (Fig. 12). We recognize that the whole-rock composition of the Kaskanak granodiorite from which titanite was analyzed is not likely representative of the melt in equilibrium with titanite during its growth, and thus our calculated partition coefficients are approximate. We infer that our titanite partition coefficients are relatively accurate for the REEs and HFSEs where the concentrations in titanite are much greater than the melt and are underestimated for compatible elements (e.g., Sr, Sc) that occur dominantly in other major mineral phases (e.g., plagioclase, amphibole, and magnetite).

This is a preprint, the final version is subject to change, of the American Mineralogist (MSA)
Cite as Authors (Year) Title. American Mineralogist, in press.
(DOI will not work until issue is live.) DOI: http://dx.doi.org/10.2138/am-2017-6053

Model b – differentiation of the Kaskanak batholith. Rayleigh fractionation described in model b addresses the second stage of low temperature differentiation of the Kaskanak granodiorite to produce the observed compositional range of granodiorite and granite porphyries. The best fit for model b ($\sum(R^2) = 2.9$) produces residuals within 0 –10% of the observed daughter composition for most of the selected trace elements (Table 4). The model estimates 16-20 wt.% crystal fractionation of a bulk composition of 61.2 wt.% amphibole, 28.0 wt.% plagioclase, 2.7 wt.% magnetite, 6.2 wt.% apatite, 1.8 wt.% titanite, and 0.07 wt.% zircon (Fig. 14). The most differentiated granodiorite porphyry and quartz granite porphyry compositions shown in Figure 14f may also require additional apatite and allanite fractionation to suppress the LREE.

Eu and Ce anomalies revisited. A conclusion that results from the modeling is that fractionation of titanite, and to a lesser degree amphibole or apatite, can cause the Eu anomaly of the bulk rock to change from a small negative anomaly ($Eu/Eu^* < 1$) to a small positive anomaly ($Eu/Eu^* > 1$) because the fractionating assemblage incorporates REE^{3+} preferentially to Eu^{2+} (Fig. 14f). In general, positive Eu anomalies are not observed from whole-rock compositions, however; except for the modest positive anomalies in the most differentiated leucocratic granite porphyry dikes (Fig. 8d). Since a majority of the Eu in the melt occurs as Eu^{2+} over the range of natural oxygen fugacities of volcanic arc melts (e.g., Wilke and Behrens, 1999), a likely explanation for this discrepancy between observed and modeled Eu contents is the oxidation of Eu^{2+} to Eu^{3+} in highly oxidized systems (Dilles et al., 2015) so that additional Eu^{3+} is incorporated by titanite. Note that the abundance of Eu or Ce in the melt is miniscule compared to the abundance of other oxidizing and reducing species and when the REE^{3+} are highly suppressed by titanite fractionation, a change in the Eu^{2+}/Eu^{3+} or Ce^{4+}/Ce^{3+} ratios would not

This is a preprint, the final version is subject to change, of the American Mineralogist (MSA)
Cite as Authors (Year) Title. American Mineralogist, in press.
(DOI will not work until issue is live.) DOI: http://dx.doi.org/10.2138/am-2017-6053

likely facilitate a change the oxidation state of the melt (i.e. the oxidation state of the melt is buffered). The likely result is that some of the remaining Eu^{2+} and Ce^{4+} is converted to a 3^{+} valence by equilibration with the melt. This affect would buffer the Eu anomaly of the melt near neutrality in oxidized systems, and could potentially decrease the Ce anomaly recorded in zircons (Fig. 10d) as titanite would diminish the partitioning of Ce^{3+} into zircon. Additional factors that could affect the oxidation state of the melt and the observed zircon Eu and Ce anomalies include the addition of new oxidizing or reducing species such as $Fe^{(2+,3+)}$ or $S^{(2-,4+,6+)}$ via assimilation of wall rocks or by the introduction of new melt by convection or recharge (Chambefort et al., 2008; 2013). Additionally, late-stage breakdown of magmatic anhydrite or sulfate bearing melt species to liberate SO_2 as a volatile species could increase the oxidation state of the melt (Dilles et al., 2015). Each of these scenarios are important to consider when critically evaluating the potential fertility of a given melt based on these redox-sensitive proxies.

Late Cretaceous petrogenesis and fertility

Late Cretaceous plutonic rocks in the Pebble district have a >300 km^2 areal extent and upper crustal volumes likely exceeding 1,500 km^3. They represent one of the best delineated Cretaceous igneous complexes identified in the SW Alaska Range. Major and trace element geochemistry, petrographic evidence, Ti-in-zircon estimates, and redox-sensitive proxies (e.g., zircon Eu anomalies, whole-rock V/Sc ratios) document evolution over a ~10 m.y. period from early, high-temperature, intermediate composition, moderately oxidized and hydrous melts to late low-temperature, silicic composition, and strongly oxidized and hydrous melts associated with ore formation. The earliest (~99-98 Ma) pre-mineral intrusions of diorite and monzodiorite contain minorly differentiated to intermediate SiO_2 contents, crystallized at relatively high

This is a preprint, the final version is subject to change, of the American Mineralogist (MSA)
Cite as Authors (Year) Title. American Mineralogist, in press.
(DOI will not work until issue is live.) DOI: http://dx.doi.org/10.2138/am-2017-6053

805 temperatures (~930-730°C Ti-in-zircon, Fig. 10), included both calc-alkaline and alkaline
806 compositions, and were only modestly hydrous and oxidized (e.g., pyroxene-biotite-magnetite ±
807 amphibole-bearing and likely ilmenite-poor or -free). The youngest and most evolved alkaline
808 intrusions include monzonite porphyry dikes that contain magnetite and titanite assemblages
809 reflecting more strongly oxidized conditions (Wones, 1989). By the end of pre-mineral
810 magmatism at ~95 Ma, parental melts had evolved to form the calc-alkaline hornblende-biotite
811 granodiorite sills. The abundant amphibole in these sills indicates an evolution towards higher
812 (≥4 wt.%) water contents. Eu/Eu* anomalies and large Ce/Nd ratios of zircons in the
813 granodiorite sills indicate they were both highly oxidized and hydrous enough to suppress early
814 plagioclase fractionation (Ballard et al., 2002; Dilles et al., 2015).
815 After an approximately 4 m.y. magmatic gap, the Kaskanak batholith was emplaced
816 between 91-89 Ma. Early phases include equigranular granodiorite and serval small porphyritic
817 andesite dikes that were followed by a succession of more evolved porphyries which were
818 emplaced contemporaneously with ore formation (Lang et al., 2013; Olson, 2015). The Kaskanak
819 batholith makes up more than 60% of the footprint of Late Cretaceous plutonic rocks currently
820 mapped in the Pebble district and has an inferred volume of ~900 km^3. If the northern contact of
821 the batholith were extended beneath cover 25 km further to the northeast as proposed by
822 Anderson et al. (2014) based on 3D inverse magnetic modeling, then the volume could be
823 significantly larger (3-5x). Where the Kaskanak batholith is mapped, it is dominated by a mineral
824 assemblage of hornblende, plagioclase, quartz, magnetite, and titanite. Together, this assemblage
825 requires strongly hydrous and oxidized conditions that are notably consistent with the small Eu
826 anomaly and large Ce anomaly of zircons. Zircon and titanite geothermometry indicate that these
827 minerals crystallized at low temperatures of 680 to 800 °C similar to Ti-in-zircon temperatures

828 estimates of other porphyry magmas (Dilles et al., 2015), and are consistent with differentiation
829 of Kaskanak granodiorite to granite porphyry by the fractionating assemblage defined in model b
830 (Table 3) which includes titanite. Ore-forming fluids are therefore closely associated with low-
831 temperature and crystal-rich magma, and consistent with fluid saturation and separation from
832 magma via cooling and crystallization (Burnham, 1979).

833 The long lifespan and potentially the fertility of the Kaskanak batholith requires periodic
834 injections of hot melts. Evidence for such injections are directly recorded in the trace element
835 variations and Zr-in-titanite temperature increases in zones with low Y <2000 (see Figs. 11 and
836 12). Hornblende rims are also commonly zoned (Fig. 11b) and have implications for the
837 pressures (i.e., depth) of crystal growth and the rate of cooling upon final emplacement. Zoned
838 hornblende is uncommon for plutonic igneous rocks where hornblende zonations may diffuse
839 and homogenize when held at magmatic temperatures for extended periods of time (e.g.,
840 Houston and Dilles, 2013). Instead, these zoned amphiboles also are supportive of periodic
841 injections of melt into the shallow crust where the melt cooled relatively rapidly to preserve
842 these textures.

843 The overall progressive evolution of Kaskanak batholith to more silicic compositions
844 starts from early small volumes of andesite to a dominant volume of granodiorite to late small
845 volumes of granite and subordinate andesite. This progression suggests that melt injections were
846 primarily dacitic and progressively more differentiated with time. There is no clear evidence for
847 Cretaceous basaltic magmas in the upper crustal environment exposed today, and subordinate
848 porphyritic andesite dikes are the only intermediate magmas exposed that were emplaced
849 contemporaneously with the Kaskanak batholith. Nonetheless, it is likely that primitive hydrous
850 basalt or andesite melts contributed water, ore metals, and sulfur to the silicic melts of the

This is a preprint, the final version is subject to change, of the American Mineralogist (MSA)
Cite as Authors (Year) Title. American Mineralogist, in press.
(DOI will not work until issue is live.) DOI: http://dx.doi.org/10.2138/am-2017-6053

Kaskanak batholith leading to the formation of one of the largest porphyry Cu-Au-Mo deposits in the world. We infer that the transfer of components from mafic to silicic melts via assimilation-fractional crystallization and recharge in a MASH or hot zone likely occurred in the deep crust. The low La/Yb and modest Sr/Y ratios suggest the MASH zone was in the base of thin crust (<30 km), and the high temperature fractionating assemblage (model a) had a composition equivalent to hornblende gabbro, which requires water-rich melts.

Implications

Protracted magmatic activity is a common feature of porphyry copper mineral belts where mineralized intrusions are commonly the culmination of long-lived magmatic activity (Seedorff et al., 2005; Chiaradia et al., 2009; Sillitoe, 2010; Richards, 2011). In the Pebble district, magmatic activity spanned ~10 m.y. and culminated over the last 2 m.y. with the emplacement of the Kaskanak batholith (Lang et al., 2013; Olson, 2015). Increased fertility associated with protracted magmatism in the Pebble district may be related to increased subduction components (e.g., water) supplied to the mantle wedge to promote partial melting. The initial hydrous, relatively oxidized, and potentially sulfate-rich (cf., Chambefort et al., 2008, 2013) basaltic melts likely included both alkaline and calc-alkaline compositions. They probably differentiated in the lower- to mid-crustal MASH or hot zones via fractionation and early removal of magnetite and amphibole and partial suppression of plagioclase to produce cooler highly oxidized, hydrous calc-alkaline andesite to dacite melts that ascended to the middle and upper crust.

Pebble, together with Grasberg, Bingham, and Kerr-Sulphurets-Mitchell, are among a handful of large porphyry deposits that have large endowments of copper, gold and

This is a preprint, the final version is subject to change, of the American Mineralogist (MSA)
Cite as Authors (Year) Title. American Mineralogist, in press.
(DOI will not work until issue is live.) DOI: http://dx.doi.org/10.2138/am-2017-6053

874 molybdenum. Seedorff et al. (2005) noted this porphyry metal association for both monzonitic
875 Cu (Mo-Au) and tonalitic-granodioritic Cu-(Au-Mo) magma compositions and noted gold
876 associated with syenitic and dioritic magma compositions. Gold-rich porphyry deposits are
877 therefore broadly correlated with alkalic and intermediate composition magmas, which is the
878 case at Pebble, Bingham, and Kerr-Sulpherets-Mitchell. Molybdenum, however, is well-known
879 to be enriched in porphyry deposits that have more evolved melt compositions.

880 Why Pebble is both a gold-rich (~0.3 ppm) and molybdenum-rich (~250 ppm) porphyry
881 copper deposit is not completely resolved, but some inferences can be made. Many of the
882 porphyry, epithermal, and intrusion-related deposits hosted in the volcanic arc crust of the
883 Wrangellia composite terrane of southern Alaska are commonly gold-rich, so Pebble is not
884 unique. We propose that chalcophile element enrichment of both copper and gold is inherent of
885 the highly-oxidized hydrous and sulfur-rich basalt magmas where oxidized conditions stabilize
886 sulfate and minimize reduced sulfur so that formation and fractionation of immiscible sulfide
887 melt is inhibited (Carroll and Rutherford, 1987, 1988; Keith et al., 1997; Tosdal et al., 2009;
888 Chambefort et al., 2008; 2013; Dilles et al., 2015). Under more reduced conditions, copper- and
889 gold-rich sulfide melt would form and potentially fractionate to reduce copper and gold contents
890 of the magma and make it infertile (Botcharnikov et al., 2013; Li and Audétat, 2013).
891 Alternatively, interactions of hydrous and oxidized basalt in the MASH zone with Triassic and
892 Jurassic mafic crystalline rocks and ultramafic cumulates may have been a possible source of
893 sulfide and trace metal enrichment. In the Kennecott district in southeast Alaska (Fig. 1), for
894 example, some of the world's highest grade copper-(silver) ores ever mined are thought to be
895 scavenged from the Triassic Nikolai Greenstone host-rocks in the Wrangellia terrane (MacKevett
896 et al., 1997). In south-central Alaska, gabbroic rocks of the Jurassic Talkeetna Arc are also

This is a preprint, the final version is subject to change, of the American Mineralogist (MSA)
Cite as Authors (Year) Title. American Mineralogist, in press.
(DOI will not work until issue is live.) DOI: http://dx.doi.org/10.2138/am-2017-6053

locally enriched in base metals such as Cr, Ni, and Cu (DeBari and Sleep, 1991; Greene et al., 2006), and in the Pebble district, gabbro roof pendants contain magmatic sulfide and bulk-compositions containing up to 50 ppm Ni and 350 ppm Cu. An identifiable crustal source for gold is elusive. Gold content is near crustal abundance and is not anomalous in the Nikolai Greenstone of the Wrangellia terrane nor in the Jurassic gabbro and basalt roof pendants and Late Cretaceous biotite pyroxenite cumulates in the Pebble district where the rocks are unaffected by significant hydrothermal alteration.

The primitive Sr and Nd isotopic compositions of Pebble magmas preclude the presence of old and silicic Mo-enriched continental crust underlying much of the SW Alaska Range, except for perhaps near the suture zone. Rather, molybdenum must ultimately be derived from partial melting of the mantle wedge or from assimilation of older Mesozoic mafic to intermediate arc crust of the Peninsula terrane. Neither source is typical of porphyry deposits with abundant molybdenum. The Cretaceous pre-mineral alkalic magmas at Pebble may have provided Mo-enrichment to the crust because alkalic magmas are commonly enriched in Mo (Carten et al., 1993; Seedorff et al., 2005). Nonetheless, both the long-time scale of igneous processes, and the strong differentiation from inferred hydrous basalt to andesite and mineralizing granodiorite to granite melts would have enriched Mo in end-stage granite porphyry intrusions because of the incompatible behavior of Mo in melts (Candela and Holland, 1986). The requirement of multiple events of hot silicic melt recharge followed by cooling and crystallization would have additionally enriched Mo in the latest melts.

The Pebble deposit therefore appears to have formed via relatively typical arc-magmatic processes developed in relatively thin and primitive mafic to intermediate crust. It is related to strongly oxidized hydrous magmatism that extended over a period of 10 m.y. Episodic magma

recharge, and assimilation and fractional crystallization are implicated in production of late-stage granodiorite to granite melt compositions with inferred elevated water, sulfur, chlorine, Cu, Au, and Mo contents. Cooling and crystallization led to further magmatic differentiation and emplacement of multiple generations of porphyry dikes with each episode accompanied by magmatic-derived ore fluids. These implications are largely inferred from whole-rock trace element and isotope geochemistry, mineral geochemistry, and crystal fractionation modeling constrained by petrographic observations.

Acknowledgments

The authors thank the many geologists employed by the Pebble Partnership who facilitated core sampling and logging, and provided necessary logistical support for the project. We thank Matt Coble and Joe Wooden of the USGS-Stanford SHRIMP-RG lab for assistance with data processing and interpretation. We greatly thank Eric Seedorff and an anonymous reviewer for their feedback which greatly improved this manuscript. Additionally, we thank fellow OSU VIPER faculty and students for thoughtful discussions and support. This research was supported by the Pebble Partnership, and in part by NSF grants EAR-1049792 and EAR-1447730.

References

Aleinikoff, J.N., Plafker, G., and Nokleberg, W.J. (1988) Middle Pennsylvanian plutonic rocks along the southern margin of Wrangellia. In T.D. Hamilton and J.P. Galloway, Eds., The United States Geological Survey in Alaska: Accomplishments during 1987. US Geological Survey, Circular 1016, 110-113.

Aleinikoff, J.N., Farmer, G.L., Rye, R.O., and Nokleberg, W.J. (2000) Isotopic evidence for the sources of Cretaceous and Tertiary granitic rocks, east-central Alaska: Implications for the tectonic evolution of the Yukon-Tanana Terrane. Canadian Journal of Earth Sciences, 37, 945-956.

947 Amato, J.M., Bogar, M.J., Gehrels, G.E., Farmer, G.L., McIntosh, W.C. (2007a) The Tlikakila
948 Complex in southern Alaska: A supra-subduction-zone ophiolite between the Wrangellia
949 Composite terrane and North America. The Geological Society of America Special Papers,
950 431, 227-252.
951 Amato, J.M., Foley, C., Heizler, M., and Esser, R. (2007b) 40Ar/39Ar and U-Pb geochronology,
952 geochemistry, and tectonic setting of three episodes of Cretaceous-Eocene calc-alkaline
953 magmatism in the Lake Clark region, southwestern Alaska: Geological Society of America
954 Special Papers, 431, 455-475.
955 Amato, J.M., Rioux, M.E., Kelemen, P.B., Gehrels, G.E., Clift, P.D., Pavlis, T.L, and Draut,
956 A.E. (2007c) U-Pb geochronology of volcanic rocks from the Jurassic Talkeetna Formation
957 and detrital zircons from prearc and postarc sequences: Implications for the age of
958 magmatism and inheritance in the Talkeetna arc. The Geological Society of America Special
959 Papers, 431, 253-271.
960 Anderson, E.D., Zhou, W., Li, Y., Hitzman, M.W., Monecke, T., Lang, J.R., and Kelley, K.D.
961 (2014) Three-dimensional distribution of igneous rocks near the Pebble porphyry Cu-Au-Mo
962 deposit in southwestern Alaska: Constraints from regional-scale aeromagnetic data.
963 Geophysics, 79, B63-B79.
964 Annen, C., Blundy, J.D., and Sparks, R.S.J. (2006) The genesis of intermediate and silicic
965 magmas in deep crustal hot zones. Journal of Petrology, 47, 505-539.
966 Ayuso, R.A., Kelley, K.D., Eppinger, R.G., and Forni, F. (2013) Pb-Sr-Nd isotopes in surficial
967 materials at the Pebble Porphyry Cu-Au-Mo deposit, southwestern Alaska: Can the
968 mineralizing fingerprint be detected through cover? Economic Geology, 108, 543-562.
969 Bachmann, O., and Bergantz, G.W. (2008) Rhyolites and their source mushes across tectonic
970 settings. Journal of Petrology, 49, 2277-2285.
971 Bachmann, O., Dungan, M.A., and Bussy, F. (2005) Insights into shallow magmatic processes in
972 large silicic magma bodies: The trace element record in the Fish Canyon magma body,
973 Colorado. Contributions in Mineralogy and Petrology, 149, 338-349.
974 Bacon, C.R., and Druitt, T.H. (1998) Compositional evolution of the zoned calcalkaline magma
975 chamber of Mount-Mazama, Crater Lake, Oregon. Contributions to Mineralogy and
976 Petrology, 98, 224-256.
977 Bacon, C.R., Vazquez, J.A., and Wooden, J.L. (2012) Peninsular terrane basement ages recorded
978 by Paleozoic and Paleoproterozoic zircon in gabbro xenoliths and andesite from Redoubt
979 Volcano, Alaska. Geological Society of America Bulletin, 224, 24-34.
980 Ballard, J.R., Palin, J.M., and Campbell, I.H. (2002) Relative oxidation states of magmas
981 inferred from Ce(IV)/Ce(III) in zircon: Application to porphyry copper deposits of northern
982 Chile. Contributions to Mineralogy and Petrology, 144, 347-364.
983 Barker, F. (1987) Cretaceous Chisana island arc of Wrangellia, eastern Alaska. Geological
984 Society of America Abstracts with Programs, 19, 580.
985 Barnes, D.F. (1977) Bouguer gravity map of Alaska. US Geological Survey Map, GP-913,
986 1:250,000. Available: http://pubs.er.usgs.gov/publication/gp913/.
987 Beard, J.S., and Barker, F. (1989) Petrology and tectonic significance of gabbros, tonalities,
988 shoshonites, and anorthosites in a late Paleozoic arc-root complex in the Wrangellia terrane,
989 southern Alaska. Journal of Geology, 97, 667-683.
990 Black, L.P., Kamo, S.L., Allen, C.M., Aleinikoff, J.N., Davis, D.W., Korsch, R.J, and Foudoulis,
991 C. (2003) TEMORA 1: a new zircon standard for Phanerozoic U-Pb geochronology.
992 Chemical Geology, 200, 155-170.

993 Botcharnikov, R.E., Holtz, F., Mungall, J.E., Beermann, O., Linnen, R.L., and Garbe-Schönberg,
994 D. (2013) Behavior of gold in a magma at sulfide-sulfate transition: Revisited. American
995 Mineralogist, 98, 1459–1464.
996 Bouley, B.A., St. George, P., and Wetherbee, P.K. (1995) Geology and discovery at Pebble
997 Copper, a copper-gold porphyry system in southwest Alaska. In T.G. Schroeder, Ed.,
998 Porphyry deposits of the Canadian Cordillera of North America. Canadian Institute of
999 Mining, Metallurgy, and Petroleum Special Volume, 46, 422-435.
1000 Brooks, C.K., Henderson, P., and Rønsbo, J.G. (1981) Rare-earth Partition Between Allanite and
1001 Glass in the Obsidian of Sandy Braes, Northern Ireland. Mineralogical Magazine, 44, 157-
1002 160.
1003 Burnham, C.W. (1979) Magmas and hydrothermal fluids. In H.L. Barnes, Ed., Geochemistry of
1004 hydrothermal ore deposits, 2nd ed., p. 71-136. John Wiley and Sons, New York.
1005 Burnham, C.W., and Ohmoto, H. (1980) Late stage process of felsic magmatism. In S. Ishihara,
1006 and S. Takenouchi, Eds., Granitic magmatism and related mineralization. Society of Mining
1007 Geologists of Japan , 8, 1-11.
1008 Candela, P.A. (1992) Controls on ore metal ratios in granite-related ore systems: An
1009 experimental and computational approach. Transactions of the Royal Society of Edinburgh:
1010 Earth Sciences, 83, 317-326.
1011 Candela, P.A., and Holland, H.D. (1986) A mass transfer model for copper and molybdenum in
1012 magmatic hydrothermal system: The origin of porphyry-type ore deposits. Economic
1013 Geology, 81, 1-19.
1014 Candela, P.A., and Piccoli, P.M. (2005) Magmatic processes in the development of porphyry
1015 type ore systems. Economic Geology, 100th Anniversary Volume, p. 25-37.
1016 Carroll, M.R., and Rutherford, M.J. (1987) The stability of igneous anhydrite: Experimental
1017 results and implications for sulfur behavior in the 1982 El Chichón trachyandesite and other
1018 evolved magmas. Journal of Petrology, 28, 781-801.
1019 Carroll, M.R., and Rutherford, M.J. (1988) Sulfur speciation in hydrous experimental glasses of
1020 varying oxidation state: Results from measured wavelength shifts of sulfur X-rays. American
1021 Mineralogist, 73, 845-849.
1022 Carten, R.B., White, W.H., and Stein, H.J. (1993) High-grade granite-related molybdenum
1023 systems: Classification and origin. In R.V. Kirkham, W.D. Sinclair, R.I. Thorpe, and J.M.
1024 Duke, Eds., Mineral deposit modeling. Geological Association of Canada Special Paper, 40,
1025 521-554.
1026 Chambefort, I., Dilles, J.H., and Kent, J.R. (2008) Anhydrite-bearing andesite and dacite as a
1027 source for sulfur in magmatic-hydrothermal mineral deposits. Geology, 36, 719-722.
1028 Chambefort, I., Dilles, J.H., and Longo, A.A. (2013) Amphibole geochemistry of the Yanacocha
1029 Volcanics, Peru: Evidence for diverse sources of magmatic volatiles related to gold ores.
1030 Journal of Petrology, 54, 1017−1046.
1031 Chiaradia, M., Merino, D., and Spikings, R. (2009) Rapid transition to long-lived deep crustal
1032 magmatic maturation and the formation of giant porphyry-related mineralization (Yanacocha,
1033 Peru). Earth and Planetary Science Letters, 288, 505-515.
1034 Claiborne, L.L., Miller, C.F., and Wooden, J.L. (2010) Trace element composition of igneous
1035 zircon: A thermal and compositional record of the accumulation and evolution of a large
1036 silicic batholith, Spirit Mountain, Nevada. Contributions to Mineralogy and Petrology, 160,
1037 511-531.

1038 Clift, P., Draut, A., Kelemen, P.B., Blusztajn, J. and Greene, A.R. (2005) Stratigraphic and
1039 geochemical evolution of an oceanic arc upper crustal section: The Jurassic Talkeetna
1040 Volcanic Formation, south–central Alaska. Geological Society of America Bulletin, 117,
1041 902-925.
1042 Cline, J.S., and Bodnar, R.J. (1991) Can economic porphyry copper mineralization be generated
1043 by a typical calc-alkaline melt? Journal of Geophysical Research, 96, 8113-8126.
1044 Colombini, L.L., Miller, C.F., Gualda, G.A.R., Wooden, J.L., and Miller, J.S. (2011) Sphene and
1045 zircon in the Highland Range, volcanic sequence (Miocene, southern Nevada, USA):
1046 Elemental partitioning, phase relations, and influence on evolution of silicic magma.
1047 Mineralogy and Petrology, 102, 29-50.
1048 Coney, P.J., and Jones, D.L. (1985) Accretion tectonics and crustal structure in Alaska.
1049 Tectonophysics, 119, 265-283.
1050 Csejtey, B., Jr., Nelson, W.H., Jones, D.L., Silberling, N.J., Dean, R.M., Morris, M.S., Lanphere,
1051 M.A., Smith, J.G., and Silberman, M.L. (1978) Reconnaissance geologic map and
1052 geochronology, Talkeetna Mountains quadrangle, northern part of Anchorage quadrangle,
1053 and southwest corner of Healy quadrangle, Alaska. US Geological Survey Open-File Report
1054 788-558-A, 60 p., scale 1:250,000.
1055 Csejtey, B., Jr., Cox, D.P., Evarts, R.C., Stricker, G.D., and Foster, H.L. (1982) The Cenozoic
1056 Denali fault system and the Cretaceous accretionary development of southern Alaska. Journal
1057 of Geophysical Research, 87, 3741-3754.
1058 DeBari, S.M. and Sleep, N.H. (1991) High-Mg, low-Al bulk composition of the Talkeetna Arc,
1059 Alaska: Implications for primary magmas and the nature of arc crust. Geological Society of
1060 America Bulletin, 103, 37-47.
1061 Detterman, R.L., and Reed, B.L. (1980) Stratigraphy, structure, and economic geology of the
1062 Iliamna Quadrangle, Alaska. U.S. Geoplogical Survey Bulletin, 1368-B, 86 p.
1063 Detterman, R.L., Case, J.E., Miller, J.W., Wilson, F.H., and Yount, M.E. (1996) Stratigraphic
1064 framework of the Alaska Peninsula. U.S. Geological Survey Bulletin, 1969-A, 74 p.
1065 Available: http://dggs.alaska.gov/pubs/id/3754/.
1066 Dilles, J. H. (1987) The petrology of the Yerington batholith, Nevada: Evidence for the evolution
1067 of porphyry copper ore fluids. Economic Geology, 82, 1750-1789.
1068 Dilles, J.H., Kent., A.J.R., Wooden, J.L., Tosdal, R.M., Koleszar, A., Lee, R.G., and Farmer,
1069 L.P. (2015) Zircon compositional evidence for sulfur-degassing from ore-forming arc
1070 magmas. Economic Geology, 110, 241-251.
1071 Ewart, A., and Griffin, W.L. (1994) Application of Proton-Microprobe Data to Trace-Element
1072 Partitioning in Volcanic-Rocks. Chemical Geology, 117, 251-284.
1073 Faure, G. (1998) Principles and applications of geochemistry. 2nd ed., p. 335-338. Prentice Hall,
1074 New Jersey.
1075 Ferry, J.M., and Watson, E.B. (2007) New thermodynamic models and revised calibrations for
1076 the Ti-in-zircon and Zr-in-rutile thermometers. Contributions to Mineralogy and Petrology,
1077 154, 429-437.
1078 Fujimaki, H. (1986) Partition-coefficients of Hf, Zr, and REE between zircon, apatite, and liquid.
1079 Contributions to Mineralogy and Petrology, 94, 42-45.
1080 Gardener, M.C., Bergman, S.C., MacKevett, E.M., Jr., Plafker, G., Cambell, R.C., Cushing,
1081 G.W., Dodds, C.J., and McClelland, W.D. (1988) Middle Pennsylvanian pluton stitching of
1082 Wrangellia and the Alexander Terrane, Wrangell Mountains, Alaska. Geology, 15, 967-971.

1083 Gaunt, J.D., Rebaliati, C.M., Lang, J.R., Titley, E., Melis, L., Barratt, D., and Hodgson, S. (2010)
1084 Technical report on the 2009 program and update on mineral resources and metallurgy,
1085 Pebble copper-gold-molybdenum project, Alaska, 195 p. Available: http://www.sedar.com/.
1086 Glazner, A., Coleman, D., and Bartley, J. (2008) The tenuous connection between high-silica
1087 rhyolites and granodiorite plutons. Geology, 36, 183-186.
1088 Goldfarb, R.J., Ayuso, R., Miller, M.L., Ebert, S.W., Marsh, E.E., Petsel, S.A., Miller, L.D.,
1089 Bradley, D., Johnson, C., and McClelland, W. (2004) The Late Cretaceous Donlin Creek
1090 Gold Deposit, Southwest Alaska: Controls on epizonal ore formation. Economic Geology,
1091 99, 643-671.
1092 Goldfarb, R.J., Anderson, E., and Hart, C.J.R. (2013) Tectonic setting of the Pebble and other
1093 copper-gold-molybdenum porphyry deposits within the evolving middle Cretaceous
1094 continental margin of northwestern North America. Economic Geology, 108, 405-419.
1095 Gregory, M.J. (2017) A fluid inclusion and stable isotope study of the Pebbly porphyry copper-
1096 gold-molybdenum deposit, Alaska. Ore Geology Reviews, 80, 1279-1303.
1097 Gregory, M.J., Lang, J.R., Gilbert, S., and Hoal, K.O. (2013) Geometallurgy of the Pebble
1098 Porphyry Copper-Gold-Molybdenum Deposit, Alaska: Implications for gold distribution and
1099 paragenesis. Economic Geology, 108, 463-482.
1100 Greene, A.R., DeBari, S.M., Kelemen, P.B., Blusztajn, J., and Clift, P.D. (2006) A detailed
1101 geochemical study of island arc crust: The Talkeetna Arc section, south-central Alaska.
1102 Journal of Petrology, 47, 1051-1093.
1103 Grimes, C.B., Wooden, J.L., Cheadle, M.J., and John, B.E. (2015) “Fingerprinting” tectono-
1104 magmatic provenances using trace elements in igneous zircon. Contributions to Mineralogy
1105 and Petrology, 170, 5-6, 1-26.
1106 Hampton, B.A., Ridgway, K.D., and Gehrels, G.E. (2010) A detrital record of Mesozoic island
1107 arc accretion and exhumation in the North American Cordillera: U-Pb geochronology of the
1108 Kahiltna Basin, southern Alaska: Tectonics, 29, TC4015, 1-21.
1109 Harraden, C.L., McNulty, B.A., Gregory, M.J., and Lang, J.R. (2013) Shortwave infrared
1110 spectral analysis of hydrothermal alteration associated with the Pebble porphyry copper-gold-
1111 molybdenum deposit, Iliamna, Alaska. Economic Geology, 108, 483-494.
1112 Hart, C.J., Goldfarb, R.J., Lewis, L.L., and Mair, J.L. (2004) The Northern Cordilleran Mid-
1113 Cretaceous plutonic province: ilmenite/magnetite-series granitoids and intrusion-related
1114 mineralisation. Resource Geology, 54, 253-280.
1115 Hart, C.J., Lang, J.R., Goldfarb, R.J., and Farmer, G.L. (2010) Intrusive rocks associated with
1116 the Pebble porphyry Cu-Au-Mo deposit, southwest Alaska. Geological Society of America,
1117 Abstract #290-8, Denver Annual Meeting. Available:
1118 https://gsa.confex.com/gsa/2010AM/webprogram/Paper182738.html/.
1119 Hayden, L.A., Watson, E.B., and Wark, D.A. (2008) A thermobarometer for sphene (titanite).
1120 Contributions to Mineralogy and Petrology, 155, 529-540.
1121 Hildreth, W. and Moorbath, S. (1988) Crustal contributions to arc magmatism in the Andes of
1122 central Chile. Contributions to Mineralogy and Petrology, 98, 455-489.
1123 Hoskin, P.W., and Schaltegger, U. (2003) The composition of zircon and igneous and
1124 metamorphic petrogenesis. Reviews in Mineralogy and Geochemistry, 53, 27-62.
1125 Houston, R.A., and Dilles, J.H. (2013) Structural Geologic Evolution of the Butte District,
1126 Montana. Economic Geology, 108, 1397-1424.

1127 Hults, C.P., Wilson, F.H., Donelick, R.A., and O'Sullivan, P.B. (2013) Two flysch belts having
1128 distinctly different provenance suggest no stratigraphic link between Wrangellia composite
1129 terrane and the paleo-Alaskan margin. Lithosphere, 5, 575-594.
1130 Iriondo, A., Kunk, M.J., and Wilson, F.H. (2003) 40Ar/39Ar geochronology of igneous rocks in
1131 the Taylor Mountains and Dillingham Quadrangles in SW Alaska. U.S. Geological Survey
1132 Open-File Report, 03-0421, 32 p. Available: http://pubs.usgs.gov/of/2003/ofr-03-421/.
1133 Irvine, T., and Baragar, W. (1971) A guide to the chemical classification of the common volcanic
1134 rocks. Canadian Journal of Earth Sciences, 8, 523-548.
1135 Ishikawa, Y., Sawaguchi, T., Iwaya, S., and Horiuchi, M. (1976) Delineation of prospecting
1136 targets for Kuroko deposits based on modes of volcanism of underlying dacite and alteration
1137 halos. Mining Geology, 26, 105-117.
1138 Johnson, D.M., Hooper, P.R., and Conrey, R.M. (1999) XRF analysis of rocks and minerals for
1139 major and trace elements on a single low dilution Li-tetraborate fused bead. Advances in X-
1140 Ray Analysis, 41, 843-867.
1141 Jones, D.L., Silberling, N.J., Gilbert, W., and Coney, P. (1982) Character, distribution, and
1142 tectonic significance of accretionary terranes in the central Alaska Range. Journal of
1143 Geophysical Research, 87, 3709-3717.
1144 Jones, D.L., Silberling, N.J., and Coney, P.J. (1986) Collison tectonics in the Cordillera of
1145 western North America: Examples from Alaska. In M.P. Coward, and A.C. Ries, Eds.,
1146 Collsion tectonics. Geological Society of London, Special Publication 19, 367-389.
1147 Kalbas, J.L., Ridgeway, K.D., and Gehrels, G.E. (2007) Stratigraphy, depositional systems, and
1148 provenance of the Lower Cretaceous Kahiltna assemblage, Western Alaska Range: Basin
1149 development in response to oblique collision. Geological Society of America Special Paper,
1150 431, 307-344.
1151 Kay, S.M., and Mpodozis, C. (2001) Central Andean ore deposits linked to evolving shallow
1152 subduction systems and thickening crust. GSA Today, 11, 4-9.
1153 Keith, J.D., Whitney, J.A., Hattori, K., Ballantyne, G.H., Christiansen, E.H., Barr, D.L, Cannan,
1154 T.N., and Hook, CJ. (1997) The role of magmatic sulfides and mafic alkaline magmas in the
1155 Bingham and Tintic Mining Districts, Utah. Journal of Petrology, 38, 1679-1690.
1156 Klein, M., Stosch, H.G., and Seck, H.A. (1997) Partitioning of high field strength elements
1157 between amphibole and quartz-dioritic to tonalitic melts: An experimental study. Chemical
1158 Geology, 138, 257-271.
1159 Knaack, C., Cornelius, S. and Hooper, P. (1994) Trace element analyses of rocks and minerals
1160 by ICP-MS (Online). Available: http://environment.wsu.edu/facilities/geolab/technotes/icp-
1161 ms_method.html/ (accessed May 15, 2012). Peter Hooper GeoAnalytical Lab, Washington
1162 State University.
1163 Lang, J.R., Gregory, M.J., Rebagliati, C.M., Payne, J.G., Oliver, J.L., and Roberts, K. (2013)
1164 Geology and magmatic-hydrothermal evolution of the giant Pebble porphyry copper-gold-
1165 molybdenum deposit, southwest Alaska. Economic Geology, 108, 437-462.
1166 Large, R.R., Gemmell, J.B., Paulick, H., and Huston, D.L. (2001) The alteration box plot: A
1167 simple approach to understanding the relationship between alteration, mineralogy, and
1168 lithogeochemistry associated with volcanic-hosted massive sulfide deposits. Economic
1169 Geology, 96, 957-971.
1170 Le Maitre, R.W.B., Dudek, P., Keller, A., Lameyre, J., Le Bas, J., Sabine, M.J., Schmid, P.A.,
1171 Sorensen, R., Streckeisen, H., Woolley, A. and Zanettin, A.R. (1989) A classification of
1172 igneous rocks and glossary of terms: Recommendations of the International Union of

1173 Geological Sciences, Subcommission on the Systematics of Igneous Rocks. International
1174 Union of Geological Sciences, No. 552.3 CLA, 193 p.
1175 Loewen, M.W., and Kent, A.J.R. (2012) Sources of elemental fractionation and uncertainty
1176 during the analysis of semi-volatile metals in silicate glasses using LA-ICP-MS. Journal of
1177 Analytical and Atomic Spectrometry, 27, 1502-1508.
1178 Loucks, R.R. (2014) Distinctive composition of copper-ore-forming arc magmas. Australian
1179 Journal of Earth Sciences, 61, 5-16.
1180 Li, Y., and Audétat, A. (2013) Gold solubility and partitioning between sulfide liquid,
1181 monosulfide solid solution and hydrous mantle melts: Implications for the formation of Au-
1182 rich magmas and crust–mantle differentiation. Geochimica et Cosmochimica Acta, 118, 247-
1183 262.
1184 Lu, Y.J., Loucks, R.R., Fiorentini, M.L., McCuaig, T.C., Evans, N.J., Yang, Z.M., Hou, Z.Q.,
1185 Kirkland, C.L., Parra-Avila, L.A., and Kobussen, A. (2016) Zircon compositions as a
1186 pathfinder for porphyry Cu ± Mo ± Au deposits. Society of Economic Geologists Special
1187 Publication, 19, 329-347.
1188 MacKevett, E.M. Jr., Cox, D.P., Potter, R.W., and Silberman, M.L. (1997) Kennecott-type
1189 deposits in the Wrangell Mountains, Alaska high-grade copper ores near a basalt-limestone
1190 contact. Economic Geology, Monograph 9, 66-89.
1191 Mahood, G.A., and Hildreth, E.W. (1983) Large partition coefficients for trace elements in high-
1192 silica rhyolites. Geochimica et Cosmochimica Acta, 47, 11-30.
1193 Mattinson, J.M. (2005) U-Pb inter-laboratory calibrations using zircon samples: Application of
1194 the new CA-TIMS technique. Goldschmidt Conference Abstracts, High-Precision
1195 Geochronology, A319.
1196 Mazdab, F.K., and Wooden, J.L. (2006) Trace element analysis in zircon by ion microprobe
1197 (SHRIMPRG): technique and applications. Geochimica et Cosmochimica Acta, 70, A405.
1198 Mazdab, F.K., and Wooden, J.K. (2007) Trace element variability in titanite from diverse
1199 geologic environments. Geological Society of America, Abstracts with Programs, 39, 406.
1200 Mazdab, F.K., Johnson, D.A., and Barton, M.D. (2008) Trace element characterization of
1201 hydrothermal titanite from ion-oxide Cu-Au (IOCG) mineralization. Geochimica et
1202 Cosmochimica Acta, 72, A609.
1203 McDonough, W.F., and Sun, S.S. (1995) The composition of the Earth. Chemical Geology, 120,
1204 223-253.
1205 Míková, J., and Denková, P. (2007) Modified chromatographic separation scheme for Sr and Nd
1206 isotope analysis in geological silicate samples. Journal of Geosciences, 52, 221-226.
1207 Naney, M.T. (1983) Phase equilibria of rock forming ferromagnesian silicates in granitic
1208 systems. American Journal of Sciences, 283, 993-1033.
1209 Nokleberg, W.J., Plafker, G., and Wilson, F.H. (1994) Geology of south–central Alaska. In G.
1210 Plafker and H.C. Berg, Eds, The geology of Alaska. Geological Society of America, Boulder,
1211 Colorado, G-1, 311-366.
1212 Olson, N.H. (2015) The Geology, Geochronology, and Geochemistry of the Kaskanak Batholith,
1213 and other Late Cretaceous to Eocene magmatism at the Pebble Porphyry Cu-Au-Mo deposit,
1214 SW Alaska, 248 p. M.S. thesis, Oregon State University, Corvallis, Oregon.
1215 Pálfy, J., Smith, P.L., Mortensen, J.K., and Friedman, R.M. (1999) Integrated ammonite
1216 biochronology and U-Pb geochronometry from a basal Jurassic section in Alaska. Geological
1217 Society of America Bulletin, 111, 1537-1549.

Piccoli, P., Candela, P.A., and Ribers, M. (2000) Interpreting magmatic processes from accessory phases: titanite – a small-scale recorder of large-scale processes. In B. Barbarin, W.E. Stephens, B. Bonin, J.L. Bouchez, D.B. Clarke, M. Cuney, and H. Martin, Eds., 4th Hutton symposium. Transactions of the Royal Society of Edinburgh, Earth Science, 91, 27-267.

Plafker, G., Nokleberg, W.J. and Lull, J.S. (1989) Bedrock geology and tectonic evolution of the Wrangellia, Peninsular, and Chugach terranes along the Trans-Alaskan Crustal Transect in the northern Chugach Mountains and southern Copper River basin, Alaska. Journal of Geophysical Research, 94, 4255-4295.

Rebagliati, M., and Lang, J.R. (2015) Discovery of the Pebble porphyry Cu-Au-Mo deposit, Southwest Alaska: History and exploration methods. In D. Wood, Ed., Trifecta talks on discovery, exploration, and geometallurgy. Society of Economic Geology, Annual meeting, Halifax, Australia.

Reed, B.L., and Lanphere, M.A. (1972) Generalized geologic map of the Alaska-Aleutian Range batholith showing potassium-argon ages of the plutonic rocks. U.S. Geological Survey Misc. Field Studies Map, MF-372. Available: http://pubs.er.usgs.gov/publication/mf372/.

Reiners, P.W., Nelson, B.K., and Nelson, S.W. (1996) Evidence of multiple mechanism of crustal contamination of magma from compositionally zoned plutons and associated ultramafic intrusions of the Alaska Range. Journal of Petrology, 37, 261-292.

Ricardo, M.S.L. (2009) A comparison of deposit and regional intrusives, Pebble, Alaska, 74 p. B.S. thesis, University of Alberta, Calgary, Canada.

Richards, J.P. (1995) Alkalic-type epithermal gold deposits – a review. In J.F.H. Thompson, Ed., Magmas, fluids, and ore deposits. Mineralogical Association of Canada Short Course Series, 23, 367-400. Available: http://www.empr.gov.bc.ca/Mining/Geoscience/PublicationsCatalogue/OpenFiles/1998/Documents/OF1998-08/h3-43.pdf/.

Richards, J.P. (2011) High Sr/Y arc magmas and porphyry Cu ± Mo ± Au deposits: Just add water. Economic Geology, 106, 1075-1081.

Richards, J.P., and Kerrich, R. (2007) Special paper: Adakite-like rocks: Their diverse origins and questionable role in metallogenesis. Economic Geology, 102, 537-576.

Richards, J.P., Spell, T., Rameh, E., Razique, A., and Fletcher, T. (2012) High Sr/Y magmas reflect arc maturity, high magmatic water content, and porphyry Cu ± Mo ± Au potential: Examples from the Tethyan arcs of central and eastern Iran and western Pakistan. Economic Geology, 107, 295-332.

Rioux, M., Hacker, B., Mattinson, J., Kelemen, P., Blusztajn, J., and Gehrels, G. (2007) Magmatic development of an intra-oceanic arc: High precision U-Pb zircon and whole rock isotopic analyses from the accreted Talkeetna Arc, south-central Alaska. Geological Society of America Bulletin, 119, 1168-1184.

Rioux, M., Mattinson, J., Hacker, B., Kelemen, P., Blusztajn, J., Hanghøj, K., and Gehrels, G. (2010) Intermediate to felsic middle crust in the accreted Talkeetna Arc, the Alaska Peninsula and Kodiak Island, Alaska: An analogue for low-velocity middle crust in modern arcs. Tectonics, 29, TC3001, 1-17.

Ryerson, F.J., and Watson, E.B. (1987) Rutile saturation in magmas: Implications for Ti-Nb-Ta depletion in island-arc basalts. Earth and Planetary Science Letters, 86, 225-239.

1262 Schrader, C.M. (2001) Geochronology and geology of the Pebble Cu-Au-Mo porphyry and the
1263 Sill Au-Ag epithermal deposits, southwest Alaska, 109 p. M.S. thesis, University of Georgia,
1264 Athens.
1265 Seedorff, E., Dilles, J.H., Proffett, J.M., Jr., Einaudi, M.T., Zurcher, L., Stavast, W.J.A., Johnson,
1266 D.A., and Barton, M.D. (2005) Porphyry deposits: Characteristics and origin of hypogene
1267 features. Economic Geology, 100th Anniversary Volume, 251-298.
1268 Sillitoe, R.H. (2010) Porphyry copper systems. Economic Geology, 105, 3-41.
1269 Silberling, N.J., Jones, D.L., Monger, J.W.H., Coney, P.H., Berg, H.C., and Plafker, G. (1994)
1270 Lithotectonic terrane map of Alaska and adjacent parts of Canada. In G. Plafker, and H.C.
1271 Berg, Eds., The geology of Alaska. Geological Society of America, The geology of North
1272 America, G-1, plate 3, 1 sheet, 1:7,500,000.
1273 Snyder, D.C., and Hart, W.K. (2007) The White Mountain Granitoid Suite: Isotopic constraints
1274 on source reservoirs for Cretaceous magmatism within the Wrangellia Terrane. Geological
1275 Society of America Special Paper, 431, 379-399.
1276 Sun, S.S., and McDonough, W.F. (1989) Chemical and isotopic systematics of oceanic basalts:
1277 Implications for mantle composition and process. Geological Society of London Special
1278 Publication, 42, 313-345.
1279 Tanaka, T., Togashi, S., Kamioka, H., Amakawa, H., Kagami, H., Hamamoto, T., Yuhara, M.,
1280 Orihashi, Y., Yoneda, S., Shimizu, H., and others (2000) JNdi-1: A neodymium isotopic
1281 reference in consistency with LaJolla neodymium. Chemical Geology, 168, 279-281.
1282 Tosdal, R.M., Dilles, J.H., and Cooke, D.R. (2009) From source to sinks in auriferous magmatic-
1283 hydrothermal porphyry and epithermal deposits. Elements, 5, 289-295.
1284 Trail, D., Watson, E.B., and Tailby, N.D. (2011) The oxidation state of Hadean magmas and
1285 implications for early Earth's atmosphere. Nature, 480, 79-82.
1286 Walker, B.A., Klemetti, E., Grunder, A., Dilles, J., Tepley, F., and Giles, D. (2013) Crystal
1287 reaming during the assembly, maturation and waning of an eleven-million-year crustal
1288 magma cycle: thermobarometry of the Aucanquilcha Volcanic cluster. Contributions to
1289 Mineralogy and Petrology, 165, 663-682.
1290 Wallace, W.K., Hanks, C.L., and Rogers, J.F. (1989) The southern Kahiltna terrane: Implications
1291 for the tectonic evolution of southwestern Alaska. Geological Society of America Bulletin,
1292 101, 1389-1407.
1293 Watson, E.B., and Green, T.H. (1981) Apatite/liquid partition coefficients for the rare earth
1294 elements and strontium. Earth and Planetary Science Letters, 52, 405-421.
1295 Watson, E.B., Wark, D.A., and Thomas, J.B. (2006) Crystallization thermometers for zircon and
1296 rutile. Contributions to Mineralogy and Petrology, 151, 413-433.
1297 Webster, J.D. (1992) Water solubility and chlorine partitioning in Cl-rich granitic systems:
1298 Effects of melt composition at 2 kbar and 800ºC. Geochimica et Cosmochimica Acta, 56,
1299 679-687.
1300 Weis, D., Kieffer, B., Maerschalk, C., Barling, J., de Jong, J., Williams, G.A, Hanano, D.,
1301 Pretorius, W., Mattielli, N., Scoates, J.S. and Goolaerts, A. (2006) High-precision isotopic
1302 characterization of USGS reference materials by TIMS and MC-ICP-MS. Geochemistry,
1303 Geophysics, Geosystems, 7, 30 p.
1304 Wilke, M., and Behrens, H. (1999) The dependence of the partitioning of iron and europium
1305 between plagioclase and hydrous tonalitic melt on oxygen fugacity. Contributions to
1306 Mineralogy and Petrology, 137, 102-114.

1307 Wilson, F.H. (1985) The Meshik Arc - an Eocene to earliest Miocene magmatic arc on the
1308 Alaska Peninsula. Alaska Division of Geological and Geophysical Surveys Professional
1309 Report, 88, 14 p. Available: http://dggs.alaska.gov/pubs/id/2269/.
1310 Wilson, F.H., Hudson, T.L., Grybeck, D., Stoeser, D.B., Preller, C.C., Bickerstaff, D., Labay, K.,
1311 and Miller, M.L. (2003) Preliminary geologic map of the northeast Dillingham Quadrangle
1312 (D-1, D-2, C-1, and C-2), Alaska. U.S. Geological Survey, Open-file Report 03-105, 13 p.,
1313 scale 1:100,000. Available: http://pubs.usgs.gov/of/2003/0105/.
1314 Wilson, F.H., Hults, C.P., Mull, C.G., and Karl, S.M. (2015) Geologic map of Alaska. USGS
1315 Scientific Investigations Map 3340, 1:1,584,000. Available:
1316 https://pubs.er.usgs.gov/publicaiton/sim3340/.
1317 Wones, D.R. (1989) Significance of the assemblage titantie + magnetite + quartz in granitic
1318 rocks. American Mineralogist, 74, 744-749.
1319 Wooden, J.L., and Barth, A.P. (2010) Coupled elemental and isotopic analyses of polygenetic
1320 zircons from granitic rocks by ion microprobe, with implications for melt evolution and the
1321 sources of granitic magmas. Chemical Geology, 277, 149-159.
1322 Young, L.E., George, P.S., and Bouley, B.A. (1997) Porphyry Copper Deposits in Relation to the
1323 Magmatic History and Palinspastic Restoration of Alaska. Economic Geology, Monograph 9,
1324 306-333.

This is a preprint, the final version is subject to change, of the American Mineralogist (MSA)
Cite as Authors (Year) Title. American Mineralogist, in press.
(DOI will not work until issue is live.) DOI: http://dx.doi.org/10.2138/am-2017-6053

Table 1: Petrography of Pebble District Igneous Rocks

Lithology	Texture(s)	Primary Mineralogy (Vol. %)
Gabbro	Fine- to medium-grained and subophitic	60-70% plag (0.25-1 mm, rarely up to 5 mm), 15-20% cpx (0.5-2.5 mm), 8% mag (0.25-1.5 mm), 2% ilm (0.2-0.5 mm), acc. apa
Basalt	Hypocrystalline, porphyritic, intersertal	60-70% plag (0.2-5 mm), 10-15% glass, 5-10% mag (0.5 mm), 10% cpx (0.2-0.5 mm),
Diorite Sills	Granular to porphyritic	60% plag (0.5-1.5 mm), 15-20% gm (0.05-0.1 mm; feldspar>qtz), 10-15% primary amph or cpx & bt (1.5-3 mm), 2-1-3% mag (0.05-0.15 mm), <2% apa (0.1-1 mm), acc. zir
Monzodiorite Stocks	Seriate, poikilitic K-felds	50-55% plag (0.2-2mm), 15-20% K-felds (2-4 mm), 15% cpx (0.1-2mm), 10% primary bt (0.1-4 mm), and 2-5% mag (0.1-0.3 mm)
Biotite Pyroxenite	Cumulate cpx, intercumulate bt & mag	70% cpx (0.25-1.5 mm, sometimes as large as 7 mm), 15% bt (0.5-1.5 mm), 15% mag (0.1-0.5 mm), acc. plag (0.1 - 0.3 mm) and apa
Monzonite Porphyry	Porphyritic, albitic coronas on plag (emphasized by preferentially illite-altered cores)	50-70% cryptocrystalline gm, 25-40% plag (0.5-6 mm), 5-15% K-felds (commonly 1-2 mm, up to 10 mm), 5-10% cpx (0.5-2 mm), 5-10% primary bt (0.5 mm-1 mm), rare accessory zircon
Monzonite Porphyry w/ megacrystic K-feldspar	Porphyritic, poikilitic K-feldspar, albitic coronas on plag (emphasized by preferentially illite-altered cores)	30-50% cryptocrystalline to microcrystalline gm (up to 0.3 mm containing plag>K-felds>bt), 20% plag (2-3 mm), 20-30% K-felds (commonly 1-2 cm, up to 7 cm), 5-10% total mafics [bt+cpx] (0.5-4 mm), 1-2% mag (0.05-0.2 mm), <0.5% apa (0.1-0.5 mm), rare acc. tit and zir
Shoshonite Dikes	Glomeroporphyritic	40-50% plag (0.5-1.5 mm), 15-20% gm (0.1-0.2 mm plag + K-felds), 10-15% cpx (1-2 mm), 5-8% mag (0.5-0.1 mm), 5-10% bt (0.5-3 mm), acc. apa (<0.3 mm)
Granodiorite Sills	Granular to porphyritic, some sieve-textured plag with albitic coronas	40-50% plag (0.5-2 mm), 30-40% aplitic gm (0.05 mm), 5-10% amph/bt (1-3 mm), 2% mag (0.1-0.3 mm), 0-1% qtz phenocrysts (0.5-1 mm), ≤1% apa (<0.1 mm), acc. zir
Porphyritic Andesite Dikes	Porphyritic, cryptocrystalline gm in 1 Gold Zone, micro-crystalline gm near 308 Zone, sieve-textured plag with albitic coronas	**1 Gold Zone:** 50-60% plag (0.1-0.5 mm), 20% cryptocrystalline gm, 8-10% amph (0.1-1 mm), 1-2% mag (0.02-0.1 mm), acc. apa **308 Zone:** 45% plag (0.5-3 mm), 35-45% fine gm (plag>K-spar>amph) (0.01-0.05 mm), 10-12% amph (1-7 mm), 2-3% mag (0.02-0.1 mm), acc. apa, zir, microcline (0.5-1 mm)
Kaskanak Granodiorite	Hypidiomorphic-granular, poikilitic K-felds, consertal qtz, early bt occurs dominantly as inclusions in amph with reaction rims, ilm only occurs as inclusions in bt	50-60% plag (0.5-3 mm), 15-20% K-felds (1-20+ mm), 10-12% amph (1-5 mm), 5-10% qtz (0.25-1.5 mm), 2-3% mag (0.5-1 mm), up to 1% primary bt (0.2-2 mm), and accessory ilm (<0.2 mm), tit (0.3-1 mm), zir (50-120 µm), and apa (50-300 µm). Note: microprobe analyses on plag yield andesine, and analyses of amph yield low-Al magnesio-hornblende.
Transitional Granodiorite	Porphyritic with consertal and graphic qtz + K-felds interstitially (0.3-1 mm), lacks significant gm (≤15%), hiatal amph phenos	50-65% plag (0.5-5 mm), 8-10% amph (commonly 1- 3 mm, up to 10 mm), variably 5-15% aplitic gm (>0.2 mm), 10% K-felds (0.3-20 mm), 5-10% interstitial quartz (0.25-1 mm), tr-3 % qtz phenocrysts (0.5-1 mm), 1-2% mag (0.5-1 mm), and acc. tit (0.3-1 mm), apa, and zir
Granodiorite Porphyry	Porphyritic with medium aplitic gm (0.1-0.3 mm)	55-60% plag (0.3-3 mm), 20% medium aplitic gm (0.1-0.3 mm), 8-10% amph (0.5-4 mm), 1-2% mag (0.2-0.5 mm), and acc. rare qtz phenocrysts (0.25-0.5 mm), apa, zir, tit
Quartz Granite Porphyry	Porphyritic with variable amounts of fine (aphanitic) aplitic gm (0.02-0.05 mm), except in 38 & 308 zones: fine to medium aplitic gm (0.05-0.15 mm)	40-60% (0.5-4 mm) plag, 25-50% fine aplitic gm (0.02-0.05 mm), 5-8% amph (commonly 0.5-2 mm, up to 5 mm), 0-2% (0.5-1.5 mm) qtz phenocrysts, and 0-5% K-spar phenocrysts (2-3 mm), acc. mag (0.2-0.5 mm), zir, apa, tit (0.3-1.2 mm)
Leucocratic Granite Porphyry	Porphyritic with coarse aplitic gm (0.1-0.3 mm)	45-50% coarse aplitic gm (0.1-0.3 mm), 35-40% plag (2-5 mm), 2-3% qtz (1-3 mm), 2-3% K-felds (3-5 mm), 2-3% mag (0.25-0.5 mm), 2-3% amph pseudomorphs (0.5-1 mm), acc. apa and zir
Paleocene Dacite Dikes	Porphyritic, weak flow banding, microcrystalline to cryptocrystalline gm (<0.01 mm)	95% gm (<0.01 mm - feldspar>>HT bt), 5% plag (0.1- 2 mm), acc. mag, apa, zir
Paleocene Andesite Dikes	Porphyritic, sieve-textured plag with albitic coronas	65-70% gm (0.01-0.05 mm), 15% plag (0.1-1 mm), 15% acicular amph (0.2-5 mm), mag (3-4%) (0.02-0.03 mm), acc. apa, zir
Paleocene-Eocene Basaltic Andesite Dikes	Porphyritic, hypocrystalline, glass is devitrified	60% devitrified glass, 20-25%, plag (0.05-0.5 mm), 8-10% acicular amph (0.1-2.5 mm), 1-3% mag (0.02-0.5 mm), acc. apa
Eocene Koktuli Mountain Grandiorite & Alaskite	Equigranular alaskite, Hypidiomorphic-granular to seriate or porphyritic granodiorite, alaskite xenoliths and crystal cargo abundant in granodiorite	**Coarse phase (alaskite):** 70-75% anhedral K-felds (1-5 mm) 10% subhedral plag (1-3 mm), 10% consertal/graphic qtz (0.1-1 mm), 3-4% mag (0.1-0.3 mm), 2-3% acicular amph (0.5-1 mm), acc. apa, zir **Medium and fine phases (granodiorite):** 70% plag (0.2-3 mm), 10% K-felds (0.2-1 mm), 8-10% acicular amph (0.2-2 mm), 5% interstial qtz (0.2-0.5 mm), 1-2% mag (0.2-0.5 mm), acc. apa, zir

Notes: Units are listed by age from oldest to youngest. Abbreviations: acc. = acccessory, act = actinolite, amph = amphibole, apa = apatite, bt = biotite, calc = calcite, chl = chlorite, cpx = clinopyroxene, epi = epidote, gm = groundmass, hem = hematite, HT = hydrothermal, ilm = ilmenite, K-felds = K-feldspar, mag = magnetite, musc = muscovite, plag = plagioclase, qtz = quartz, smect = smectite, tit = titanite, zir = zircon

This is a preprint, the final version is subject to change, of the American Mineralogist (MSA)
Cite as Authors (Year) Title. American Mineralogist, in press.
(DOI will not work until issue is live.) DOI: http://dx.doi.org/10.2138/am-2017-6053

1325

Table 2: Sr-Nd isotopic compositions

Sample ID	Lithology	Age [a] (Ma)	Rb [b] (ppm)	Sr [b] (ppm)	$^{87}Sr/^{86}Sr$ [c]	2σ	Calc $^{87}Rb/^{86}Sr$	$^{87}Sr/^{86}Sr_i$ [d]	Sm [b] (ppm)	Nd [b] (ppm)	$^{143}Nd/^{144}Nd$ [c]	2σ	Calc $^{147}Sm/^{144}Nd$	$^{143}Nd/^{144}Nd_i$ [d]	εNd_i
GH12-314-103	Gabbro	~180	19.9	201	0.704109	18	0.2863	0.703377	3.68	12.29	0.512909	12	0.1810	0.512696	5.65
3121-1080	Diorite Sill	98.1	238.3	238	0.707368	17	2.8968	0.703668	4.46	17.42	0.512873	12	0.1547	0.512782	5.07
GH12-312-42.5	Monzonite Ppy	~95	52.6	212	0.705019	18	0.7177	0.704103	2.62	11.06	0.512887	14	0.1432	0.512803	5.48
10478-515	Monzonite Ppy	~96	146.6	103	0.708666	19	4.1184	0.703406	3.22	15.37	0.512895	13	0.1266	0.512820	5.82
3082-862	Monzonite Ppy w/ megacrystic K-feldspar	94.9	169.2	510	0.704864	20	0.9596	0.703638	3.37	14.81	0.512856	12	0.1375	0.512775	4.93
7375-3310	Granodiorite Sill	94.9	171.6	592	0.704777	18	0.8384	0.703706	4.11	18.43	0.512891	13	0.1348	0.512812	5.65
10500-650.5	Andesite Ppy	91.1	10.5	579	0.704293	16	0.0525	0.704226	3.36	14.53	0.512868	12	0.1398	0.512785	5.13
11528-1412	Kaskanak Granodiorite	91.0	43.4	650	0.703874	17	0.1931	0.703628	2.89	12.56	0.512911	14	0.1391	0.512830	6.00
7385-2410	Granodiorite Ppy	90.3	144.3	141	0.707071	17	2.9608	0.703290	2.91	11.72	0.512891	15	0.1501	0.512802	5.47
8443-1978	Quartz Granite Ppy	88.9	115.7	101	0.707853	15	3.3144	0.703620	0.68	3.13	0.512887	13	0.1313	0.512810	5.62
2047-778	Leucocratic Granitic Ppy	89.2	116	154	0.706450	16	2.1791	0.703667	0.39	2.24	0.512898	14	0.1052	0.512836	6.12
7385-2821	Paleocene Andesite Dike	64.0	44.5	965	0.704362	15	0.1334	0.704239	3.60	14.99	0.512840	14	0.1451	0.512778	4.37

a - For U-Pb ages and uncertainties, see Olson (2015). Estimated ages (~) are based on ages reported for similar intrusions.

b - Compositions determined by ICP-MS at Washington State University.

c - Measured $^{87}Sr/^{86}Sr$ were corrected for Rb interference, mass fractionation (using $^{86}Sr/^{88}Sr = 0.1194$), and internally standardized to NIST SRM987 at the University of Cape Town, South Africa (Míková and Denková, 2007). Measured $^{143}Nd/^{144}Nd$ ratios were corrected for Sm and Ce interferences, mass fractionation (using $^{146}Nd/^{144}Nd = 0.7219$), and internally standardized to JNdi-1 (Tanaka et al., 2000). An external USGS basalt standard, BHVO-2, was analyzed twice as an unknown yielding values of 0.703472 and 0.703495 for $^{87}Sr/^{86}Sr$, and 0.512987 and 0.512997 for $^{146}Nd/^{144}Nd$ which fall within reported uncertainty for the standard (0.703479±20; 0.512984±15; Weis et al., 2006). Reported 2σ uncertainties correspond to the last two significant digits of the measured ratios.

d - Initial $^{87}Sr/^{86}Sr$ and $^{143}Nd/^{144}Nd$ ratios were calculated for an age of t = 90 m.y., except for the gabbro (t = 180 m.y.) and a Paleocene andesite (t = 65 m.y.).

1326

This is a preprint, the final version is subject to change, of the American Mineralogist (MSA)
Cite as Authors (Year) Title. American Mineralogist, in press.
(DOI will not work until issue is live.) DOI: http://dx.doi.org/10.2138/am-2017-6053

Table 3: Rayleigh Fractionation Model Parameters

	La	Ce	Nd	Sm	Eu	Gd	Tb	Dy	Er	Yb	Lu	Sc	Nb	Zr	Sr	Y	P_2O_5
$Kd_{amphibole}$	0.36[a]	0.68[a]	1.6[a]	2.3[a]	1.9[a]	~2.3	2.4[a]	~2.5	~2.2	1.8[a]	1.8[a]	14[a]	2.0[b]	0.5[a]	0.62[c]	7.4[c]	~0.01
$Kd_{plagioclase}$	0.30[a]	0.22[a]	0.19[a]	0.12[a]	2.0[a]	~0.13	0.14[a]	~0.14	~0.12	0.10[a]	0.10[a]	0.01[a]	0.01[b]	0.16[a]	3.4[a]	~0.14	~0.01
$Kd_{magnetitee}$	0.66[a]	0.71[a]	0.93[a]	1.2[a]	0.91[a]	~1.3	1.3[a]	~0.9	~0.6	0.44[a]	0.30[a]	5.0[a]	0.37[b]	0.24[a]	0.01[a]	0.03[b]	~0.01
$Kd_{apatitee}$	14.5[d]	21.1[d]	32.8[d]	46.0[d]	25.5[d]	43.9[d]	~39	34.8[d]	22.7[d]	15.4[d]	13.8[d]	0.01[a]	~0.01	0.636[d]	2.1[e]	~29	~180
$Kd_{allanite}$	820[f]	635[f]	463[f]	205[f]	81[f]	130[f]	71[f]	~50	~38	8.9[f]	7.7[f]	50[g]	1.7[h]	0.29[h]	0.78[h]	95.5[h]	~0.3
Kd_{zircon}	1.14[d]	1.17[d]	1.38[d]	2.03[d]	0.85[d]	6.01[d]	~16	44.9[d]	107[d]	516[d]	689[d]	161[b]	2.09[b]	~4,470	~0.01[b]	~70	~0.3
$Kd_{titanite} \geq Tit_{max}/WR_{max}$	163	296	472	477	234	423	369	386	328	272	183	1.7	330	8.75	0.10	325	~0.3
Model (a): 12.5 wt.% crystal fractionation of the following assemblage: 54.4 wt.% amphibole, 32.5 wt.% plagioclase, 7.7 wt.% magnetite, 5.1 wt.% apatite, and 0.18 wt.% allanite																	
Bulk D	2.56	2.72	3.51	4.10	3.20	3.81	3.57	3.32	2.47	1.85	1.75	7.56	0.37	0.39	1.55	2.86	6.90
Model (b): 18 wt.% crystal fractionation of the following assemblage: 61.2 wt.% amphibole, 28.0 wt.% plagioclase,2.7 wt.% magnetite, 6.2 wt.% apatite, 1.8 wt.% titanite, and 0.07 wt.% zircon																	
Bulk D	4.16	7.13	11.59	12.91	7.54	11.76	10.61	10.73	8.78	7.35	5.77	8.24	6.33	3.69	1.37	9.04	8.38

Notes: Kd partition coefficients from: a) Bacon and Druitt (1998); b) Bachmann et al. (2005); 3) Klein et al. (1997); d) Fujimaki (1986); e) Watson and Green (1981); f) Brooks et al. (1981); g) Ewart and Griffin (1994), and h) Mahood and Hildreth (1983). Where no Kd value was available in the cited references, it is estimated and noted as approximate (~). Kd values for Zr in zircon and P_2O_5 in apatite were estimated based on stoichiometry.

This is a preprint, the final version is subject to change, of the American Mineralogist (MSA)
Cite as Authors (Year) Title. American Mineralogist, in press.
(DOI will not work until issue is live.) DOI: http://dx.doi.org/10.2138/am-2017-6053

1334

Table 4: Crystal Fractionation Models

Element	1) Andesite Ppy (GH10-213-164)	2) Kaskanak Granodiorite (11532-393)	3) Leucocratic Granite Ppy (2047-778)	Calculated Daughter (model a; 1 to 2)	Residual	Rel. %	Calculated Daughter (model b; 2 to 3)	Residual	Rel. %
Sc	17.3	7.9	0.9	7.2	-0.7	-8.9	1.9	1.0	12.4
Nb	11.05	10.39	4.12	12.02	1.63	15.7	3.61	-0.51	-4.9
Zr	103	111	66	112	1	0.7	65	-1	-0.9
Sr	725	652	154	674	22	3.4	606	452	69.3
Y	22.28	17.32	3.09	17.37	0.05	0.3	3.51	0.42	2.4
P_2O_5 (wt.%)	0.456	0.233	0.024	0.208	-0.025	-10.9	0.054	0.030	12.8
La	17.11	14.63	7.43	13.89	-0.74	-5.0	7.82	0.39	2.7
Ce	36.22	28.47	8.51	28.8	0.33	1.2	8.43	-0.08	-0.3
Nd	20.32	13.52	2.24	14.53	1.01	7.5	1.65	-0.59	-4.3
Sm	4.74	3.06	0.39	3.13	0.07	2.4	0.29	-0.10	-3.3
Eu	1.61	1.03	0.17	1.20	0.17	16.5	0.28	0.11	10.8
Gd	4.58	3.08	0.40	3.15	0.07	2.1	0.36	-0.04	-1.2
Tb	0.72	0.51	0.07	0.51	0.00	0.2	0.08	0.01	1.1
Dy	4.37	3.14	0.46	3.2	0.06	2.1	0.46	0.00	-0.1
Er	2.37	1.83	0.31	1.95	0.12	6.4	0.39	0.08	4.4
Yb	2.26	1.89	0.45	2.02	0.13	6.8	0.54	0.09	4.5
Lu	0.38	0.30	0.09	0.34	0.04	14.5	0.12	0.03	8.8
					$\sum(R^2) = 5.5$			$\sum(R^2) = 2.9$	

Notes: Calculated sum of squared residuals excludes Sr.

This is a preprint, the final version is subject to change, of the American Mineralogist (MSA)
Cite as Authors (Year) Title. American Mineralogist, in press.
(DOI will not work until issue is live.) DOI: http://dx.doi.org/10.2138/am-2017-6053

Figure Captions

Figure 1: Simplified terrane map of southern Alaska (after Silberling et al., 1994). Selected Pennsylvanian and Cretaceous radiometric ages of intrusions in the Wrangellia composite terrane (WCT) are from Iriondo et al. (2003), Amato et al. (2007b), Bacon et al. (2012), and the USGS Mineral Resources Data System (MRDS) (http://mrdata.usgs.gov/). Porphyry occurrences are from Goldfarb et al. (2013) and the MRDS, and the Kennecott copper deposit (estimated age 155-110 Ma) is from MacKevett et al., 1997). Note that earliest Cretaceous magmatism in Tosina-St. Elias belt on the seaward margin of the WCT contains no known porphyry occurrences, but the younger Nutzotin-Kluane and SW Alaska Range belts of the landward margin of the WCT contains several porphyry deposits.

Figure 2: Late Cretaceous bedrock geology map of the Pebble district (modified after Lang et al., 2013). Paleocene and Eocene hypabyssal intrusions and granitic rocks are shown where they crosscut the Late Cretaceous basement, but Paleocene – Eocene volcanic and volcaniclastic cover rocks have been removed to illustrate the basement lithology where it has been intersected by drilling.

Figure 3: A) Schematic east-west cross-section and geologic reconstruction of the Pebble district interpreted from available drill core data (Olson, 2015). Lithologies as in Figure 2 or as labeled. Intrusion geometries, crosscutting relations, and fault relationships east of the ZG fault are highly interpretative and based on scarce drill data. **B)** Summary of inferred intrusion ages based on radiometric ages and crosscutting relations.

Figure 4: Total alkalis vs. silica for igneous and sedimentary rocks in the Pebble district (after Le Maitre et al., 1989; alkaline-subalkaline division of Irvine and Baragar, 1971). Weakly altered diorite sill samples are from James Lang (written communication, 2012).

Figure 5: Selected major oxide (wt.%) and trace element (ppm) variation as a function of SiO_2 (wt.%). Samples with an Ishikawa Alteration Index > 60 (Large et al., 2001) were not included in plots of Sr and the peraluminumous index (A/NCK = molar $Al_2O_3/(Na_2O+CaO+K_2O)$). Symbols as in Figure 4.

Figure 6: Trace element spider diagrams for Late Cretaceous igneous rocks of the Pebble district normalized to N-MORB (Sun and McDonough, 1989). **A)** Early alkalic and calc-alkalic <57 wt.% SiO_2; **B)** Early alkalic and calc-alkalic >57 wt.% SiO_2; **C)** Kaskanak granodiorite and porphyritic andesite dikes; **D)** granodiorite and granite porphyries of the Kaskanak batholith.

Figure 7: Rayleigh fractionation models for crystallization of 0 to 50 wt.% hornblende (green line) and 0 to 1.0 wt.% for titanite (blue line) illustrated on plots **A)** Sr/Y vs. Y and **B)** La/Yb vs. Yb. The model uses the porphyritic andesite dike starting compositions and partition coefficients listed in Tables 3 and 4. Note that most porphyry intrusions are somewhat hydrothermally altered and have low Sr/Y ratios as a result of likely Sr loss. Nonetheless, the freshest samples have Sr/Y <65 and lie in both the adakitic and normal arc fields of Richards and Kerrich (2007). Vanadium and scandium behaviors depart from one another as illustrated in **C)** V and Sc vs. SiO_2, and **D)** V/Sc vs. SiO_2. Vanadium has incompatible behavior at elevated silica likely because of V^{4+} and

V^{5+} formed under highly oxidized magmatic conditions (see text for details). The elevated V concentrations of circled samples may likely be due to hydrothermal enrichment. Symbols as in Figure 4 or as labeled.

Figure 8: Rare earth element spider diagrams for Late Cretaceous igneous rocks of the Pebble district normalized to chondrite (McDonough and Sun, 1995). A) Early alkalic and calc-alkalic <57 wt.% SiO_2; B) Early alkalic and calc-alkalic >57 wt.% SiO_2; C) Kaskanak granodiorite and porphyritic andesite dikes; D) granodiorite and granite porphyries of the Kaskanak batholith.

Figure 9: A) Sr and Nd isotopic compositions of Mesozoic and Paleocene rocks in terranes of southern Alaska. Note the isotopic composition of the Kahiltna flysch reported by Reiners et al. (1996) is slightly more radiogenic and was not utilized in the modelling. **B)** Enlargement of Sr-Nd isotopic data illustrating two-component mixing models of mean (in 10 wt.% increments) Kahiltna flysch with a primitive composition of Kaskanak granodiorite (a), diorite sills (b), and Paleocene monzonite porphyry (c). See text for rock compositions. **C)** εNd_i vs. 1/Nd for the two-component mixing models. Mixing models suggest the Kaskanak granodiorite assimilated ≤10 wt.% of the Kahiltna flysch whereas other Late Cretaceous intrusions assimilated ≤20 wt.% Kahiltna flysch. Data from Table 2 and the following: 1) Aleinikoff et al. (2000), 2) Goldfarb et al. (2004), 3) Reiners et al. (1996), 4) Snyder and Hart (2007), 5) Amato et al. (2007a), 6) Rioux et al. (2007), 7) Rioux et al. (2010), 8) Goldfarb et al. (2013), and 9) Ayuso et al. (2013).

Figure 10: Zircon trace element data from LA-ICP-MS and SHRIMP-RG analyses. **A)** Yb/Gd vs. Th/U demonstrating suppression of the MREE with crystallization. **B)** Ti-in-zircon temperatures vs. Hf where temperatures are calculated assuming an activity ratio $a(TiO_2)/a(SiO_2)$ = 0.7 using the formulation of Ferry and Watson (2007). **C)** Eu anomaly vs Hf, using Eu anomaly calculated as $Eu/Eu^* = Eu_{CN}/[Sm_{CN}^{(1/2)} * Gd_{CN}^{(1/2)}]$ where $_{CN}$ = chondrite-normalized, and **D)** Ce/Nd vs Hf, where the Ce/Nd ratio is used as a proxy for the Ce anomaly (Ce_{CN}/Ce^*_{CN}). Eu/Eu* anomalies ≥ 0.4 are characteristic of most porphyry copper deposit occurrences (Ballard et al., 2002; Dilles et al., 2015). Symbols as in Figure 4.

Figure 11: **A)** BSE image of titanite with a resorption feature (white arrow) and overgrowth rim from the Kaskanak granodiorite implicating complicated late-stage growth of titanite rims. **B)** BSE image of hornblende from the Kaskanak granodiorite also with zoned rims. Preservation of zoning in hornblende from plutonic rocks suggests the melts cooled relatively quickly. **C)** Chondrite-normalized trace element compositions of titanite from the Kaskanak granodiorite. **D)** Representative REE and HFSE contents of titanite, zircon, and whole-rock normalized to chondrite. Chondrite values from McDonough and Sun (1995).

Figure 12: Trace element compositions of titanite rims and cores from the unaltered Kaskanak granodiorite. Colored tie-lines indicate core to rim analyses on selected titanite grains. Large variations of trace element contents and ratios at ≤2000 ppm Y are correlated with a large range of Zr-in-titanite temperatures from 700-800°C. Because of the affinity of titanite to incorporate large amounts of REE and HFSEs, the concentration of these elements is expected to decrease in melts with titanite crystallization. Dashed gray lines at 2000 ppm Y indicate the lower limit of the normal crystallization and crystal-fractionation processes where trace elements vary smoothly with Y. In comparison, complex late-stage processes at Y ≤2000 ppm include irregular

and large variations in Nb/Ta, Th/U, Dy/Yb, and locally high concentrations of Sc, Nb, Th, U, and REE. Note that Eu/Eu* increases steadily as Y decreases from 6000 to 500 ppm.

Figure 13: Age and rare earth element compositions of inherited zircons from Late Cretaceous intrusions in the Pebble district. **A)** Relative probability distribution of detrital zircons from the Kahiltna flysch in southwestern and south-central Alaska (from Hampton et al., 2010). **B)** Relative probability and histogram of inherited grain ages from Cretaceous igneous rocks in the Pebble district. **C)** Yb/Gd vs. age, **D)** Eu/Eu^*_{CN} vs. age, and **E)** Ce/Nd vs. age of inherited zircons from Cretaceous igneous rocks in the Pebble district. The range of Cretaceous zircons (red box), Paleocene zircons (blue box), and Eocene zircons (green box) from Figure 10 are shown for comparison. All grain ages shown at 2σ uncertainty.

Figure 14: Rayleigh fractionation models (a) and (b) for trace element evolution of the Kaskanak batholith using starting compositions, mineral-melt partition coefficients, and bulk compositions listed in Tables 3 and 4. Black lines show fractionation paths in 2 wt.% intervals for 1 to 14 wt.% fractionation of a high-temperature assemblage for model (a) (hornblende-plagioclase-magnetite-apatite-allanite) and 0 to 20 wt.% fractionation of a lower-temperature assemblage for model (b) (hornblende-plagioclase-magnetite-apatite-titanite-zircon). See text for details. **A)** Sr vs. Sc, **B)** Y vs. Sc, **C)** Nb vs. Sc, **D)** Zr vs. Sc, **E)** P_2O_5 vs. Sc, and **F)** chondrite-normalized REE spidergrams (McDonough and Sun, 1995) for selected rock compositions and the observed range of granodiorite to granite compositions (gray field). Symbols of observed compositions as in Figure 4. Note that early fractionation of hornblende-rich assemblage (a) provides a good fit for early differentiation, but the titanite-bearing assemblage (b) is required to produce the large observed REE and HFSE depletions observed in the most silicic late porphyries.

This is a preprint, the final version is subject to change, of the American Mineralogist (MSA)
Cite as Authors (Year) Title. American Mineralogist, in press.
(DOI will not work until issue is live.) DOI: http://dx.doi.org/10.2138/am-2017-6053

Figure 01

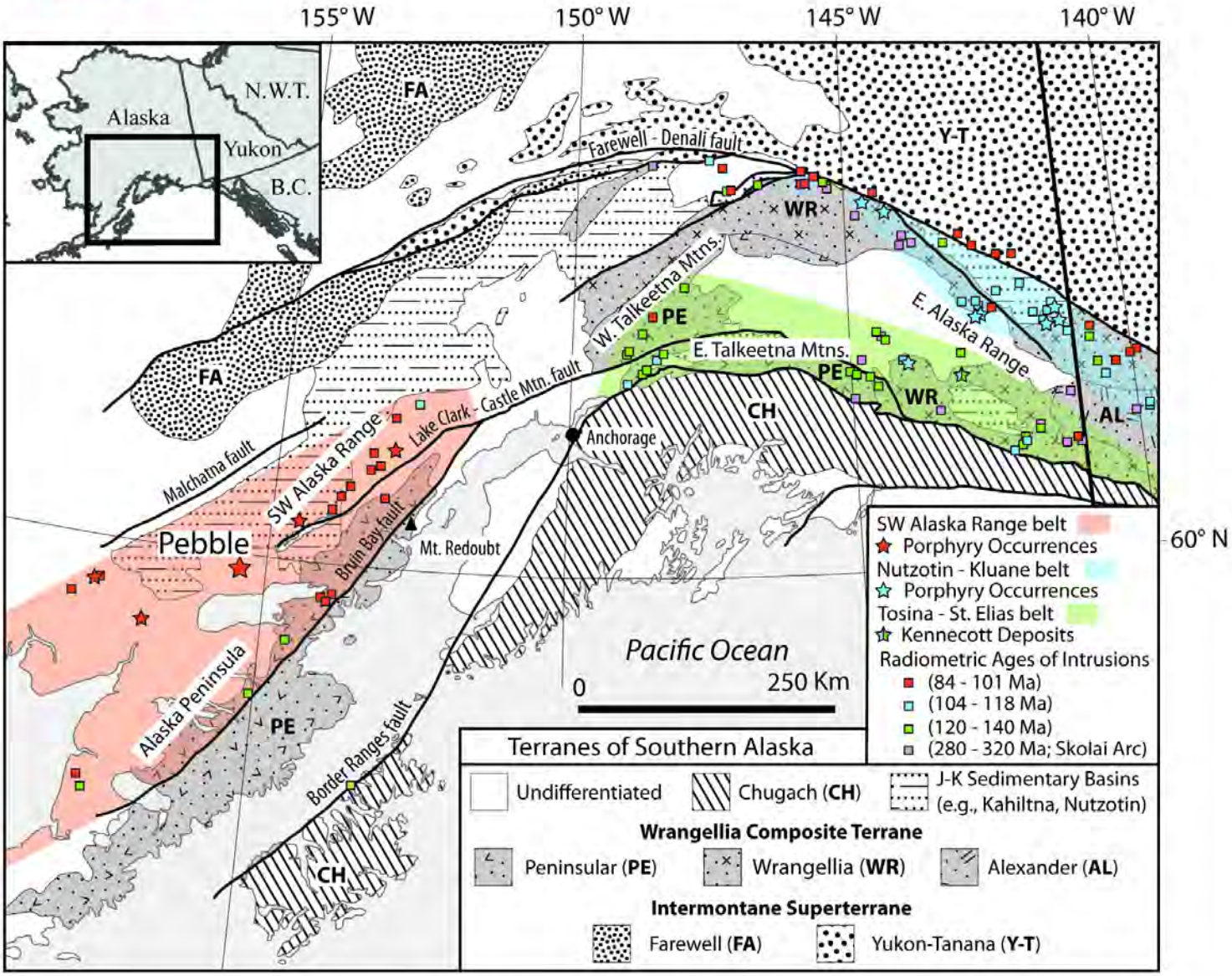

This is a preprint, the final version is subject to change, of the American Mineralogist (MSA)
Cite as Authors (Year) Title. American Mineralogist, in press.
(DOI will not work until issue is live.) DOI: http://dx.doi.org/10.2138/am-2017-6053

Figure 02

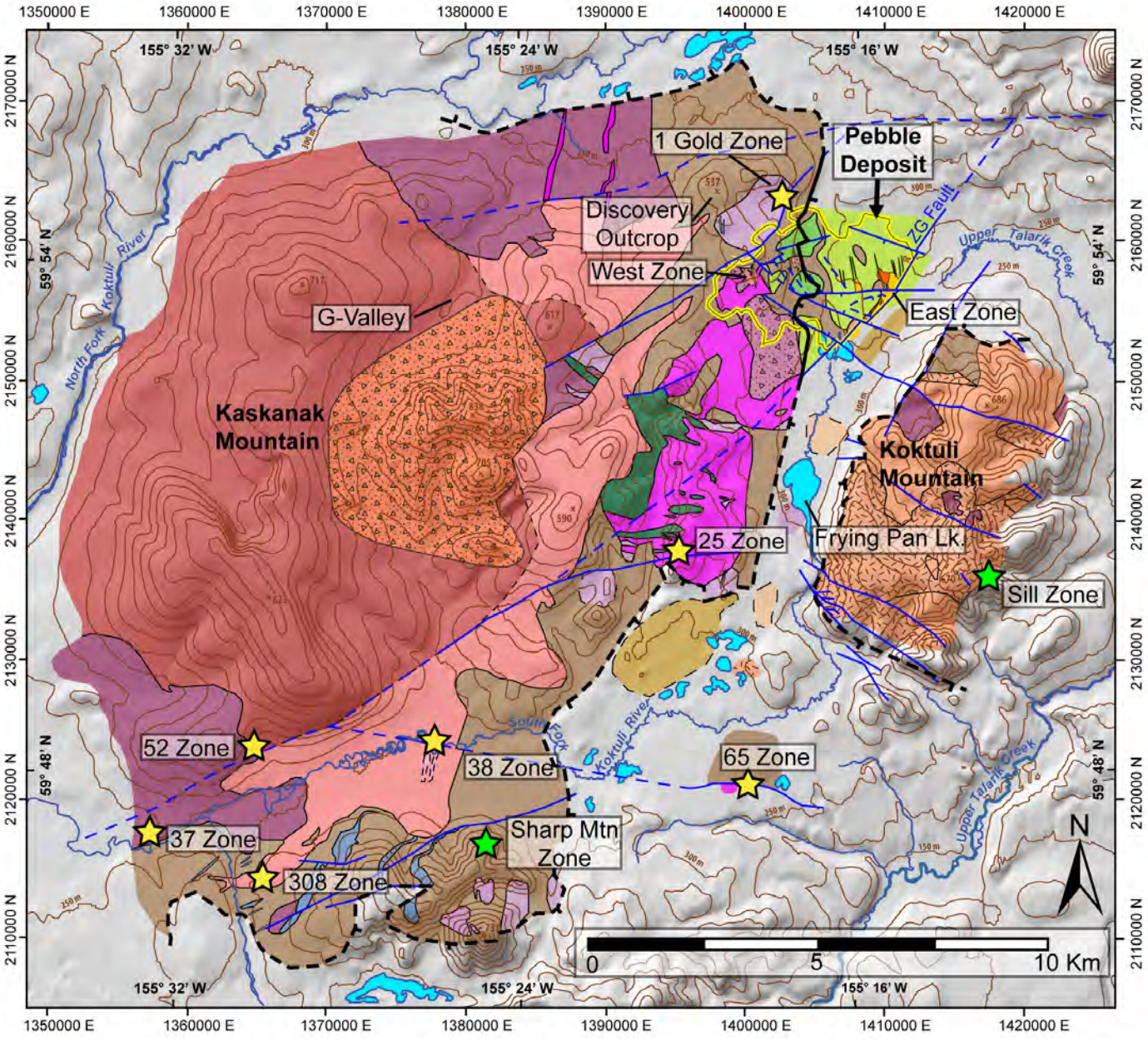

Koktuli Volcanics and Intrusions:

Eocene
- Koktuli Mountain Granodiorite & Leucogranite (Stippled)
- Latite and/or Dacite Hypabyssal Intrusions

Talarik Formation:

Paleocene
- Basaltic Andesite Hypabyssal Intrusions (age uncertain)
- Dacite Breccia

Kaskanak Batholith:

Late Cretaceous
- Leucocratic Granite Porphyry (coarse aplitic groundmass)
- Quartz Granite Porphyry (fine aplitic groundmass)
- Granodiorite Porphyry (medium aplitic groundmass)

Kaskanak Batholith (cont.):

Late Cretaceous
- Transitional Granodiorite (transitionally porphyritic)
- Kaskanak Granodiorite (equigranular)
- Porphyritic Andesite Dikes

Pre-Mineral Intrusions:

Late Cretaceous
- Granodiorite Sills
- Monzonite Magmatic/ Hydrothermal Breccia
- Monzonite Porphyry
- Monzodiorite
- Biotite Pyroxenite
- Diorite (fine and equigranular sills, porphyritic laccoliths)

Kahiltna Basin:

Jur. - Early Cret.
- Kahiltna Flysch

Intrusive Rocks:

- Gabbro and Basalt
- 0.3 wt. % Cu Equivalent Resource Boundary
- Extent of Removed Paleocene and Eocene Volcanics and Volcaniclastic Sedimentary Rocks
- Inferred Faults
- Kettle Ponds
- Topographic Contours (50-meter Intervals)
- Late Cretaceous Centers of Mineralization
- Eocene Centers of Mineralization

This is a preprint, the final version is subject to change, of the American Mineralogist (MSA)
Cite as Authors (Year) Title. American Mineralogist, in press.
(DOI will not work until issue is live.) DOI: http://dx.doi.org/10.2138/am-2017-6053

Figure 03

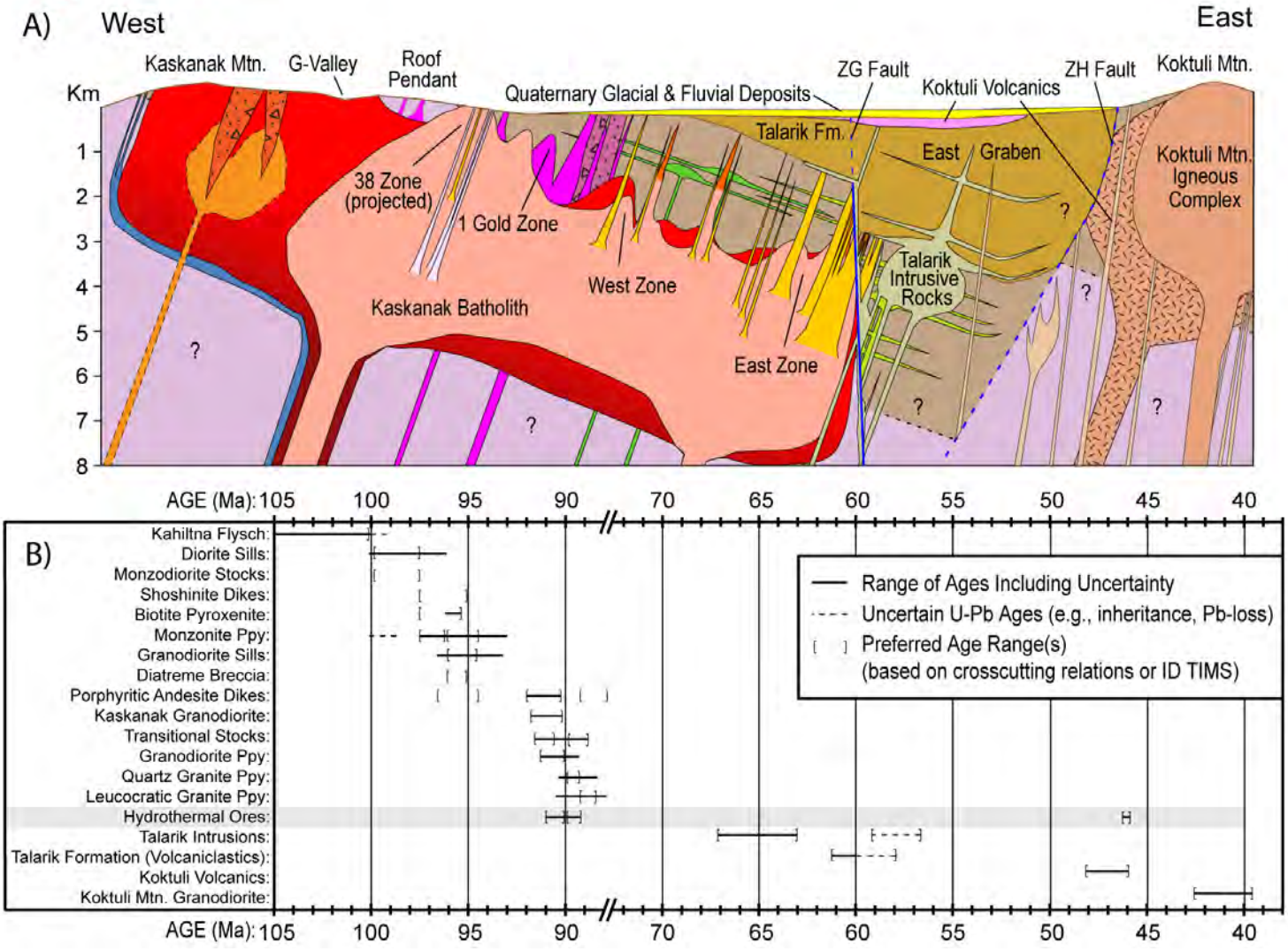

This is a preprint, the final version is subject to change, of the American Mineralogist (MSA)
Cite as Authors (Year) Title. American Mineralogist, in press.
(DOI will not work until issue is live.) DOI: http://dx.doi.org/10.2138/am-2017-6053

Figure 04

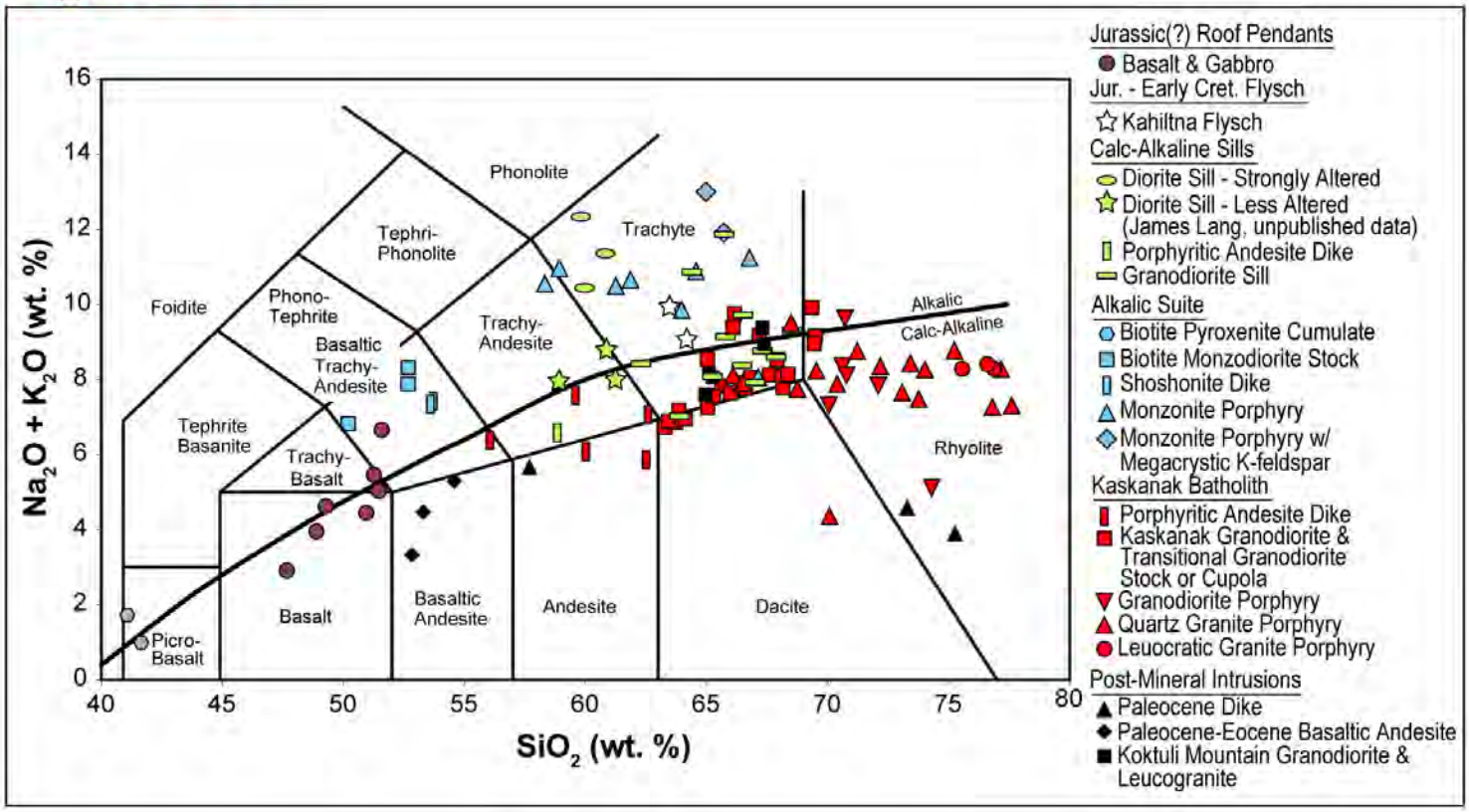

This is a preprint, the final version is subject to change, of the American Mineralogist (MSA)
Cite as Authors (Year) Title. American Mineralogist, in press.
(DOI will not work until issue is live.) DOI: http://dx.doi.org/10.2138/am-2017-6053

Figure 5

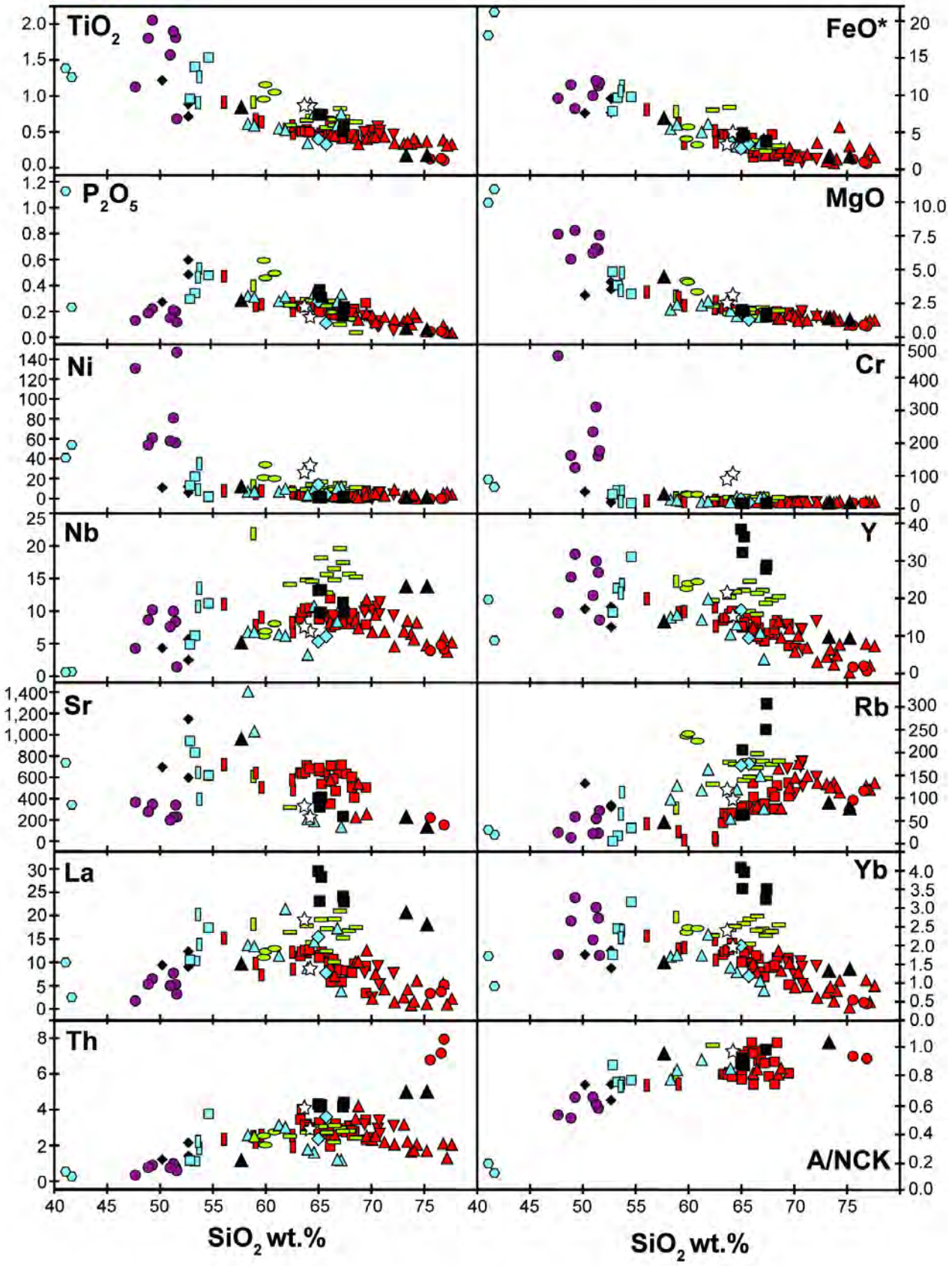

This is a preprint, the final version is subject to change, of the American Mineralogist (MSA)
Cite as Authors (Year) Title. American Mineralogist, in press.
(DOI will not work until issue is live.) DOI: http://dx.doi.org/10.2138/am-2017-6053

Figure 06

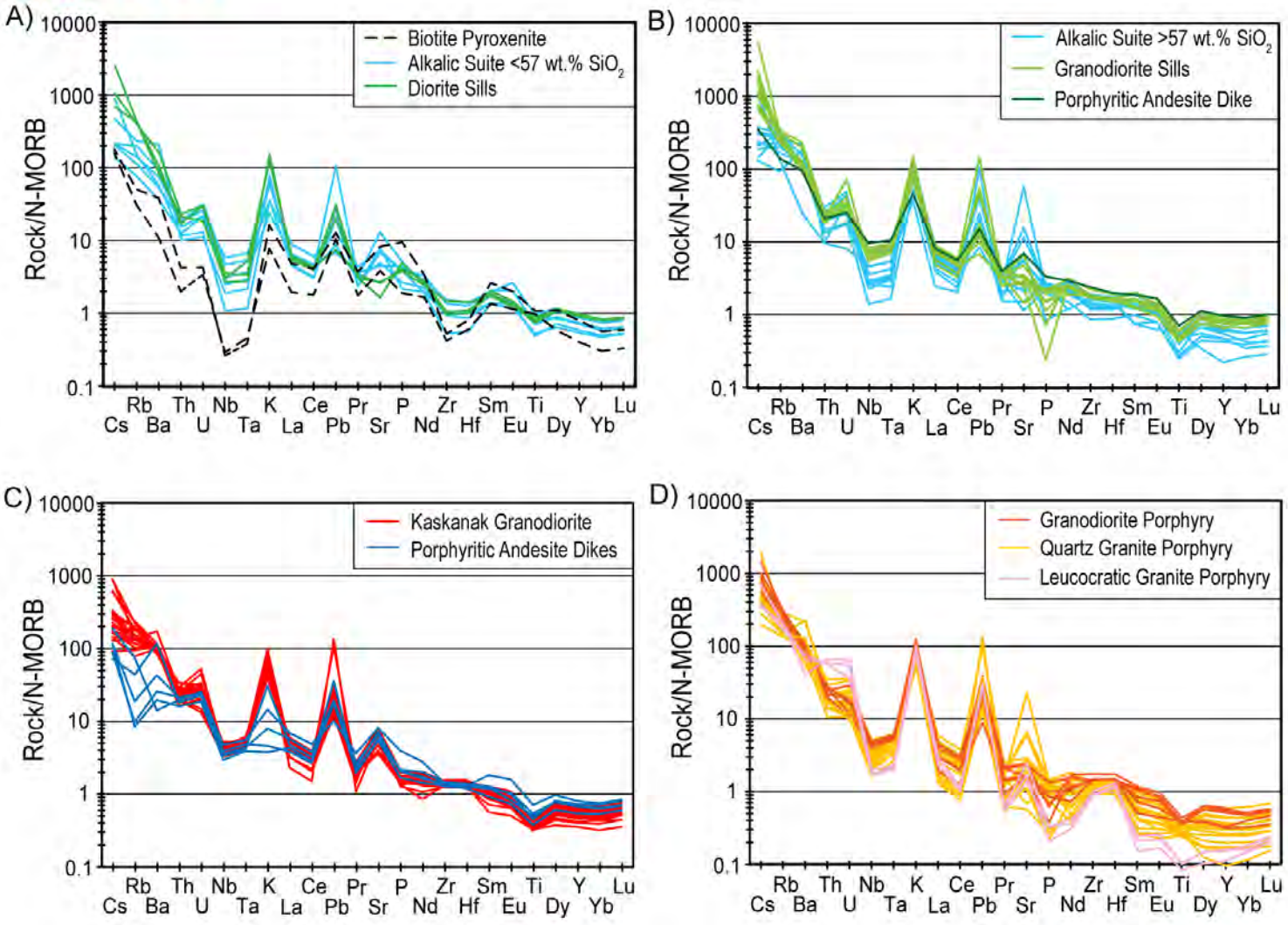

This is a preprint, the final version is subject to change, of the American Mineralogist (MSA)
Cite as Authors (Year) Title. American Mineralogist, in press.
(DOI will not work until issue is live.) DOI: http://dx.doi.org/10.2138/am-2017-6053

Figure 07

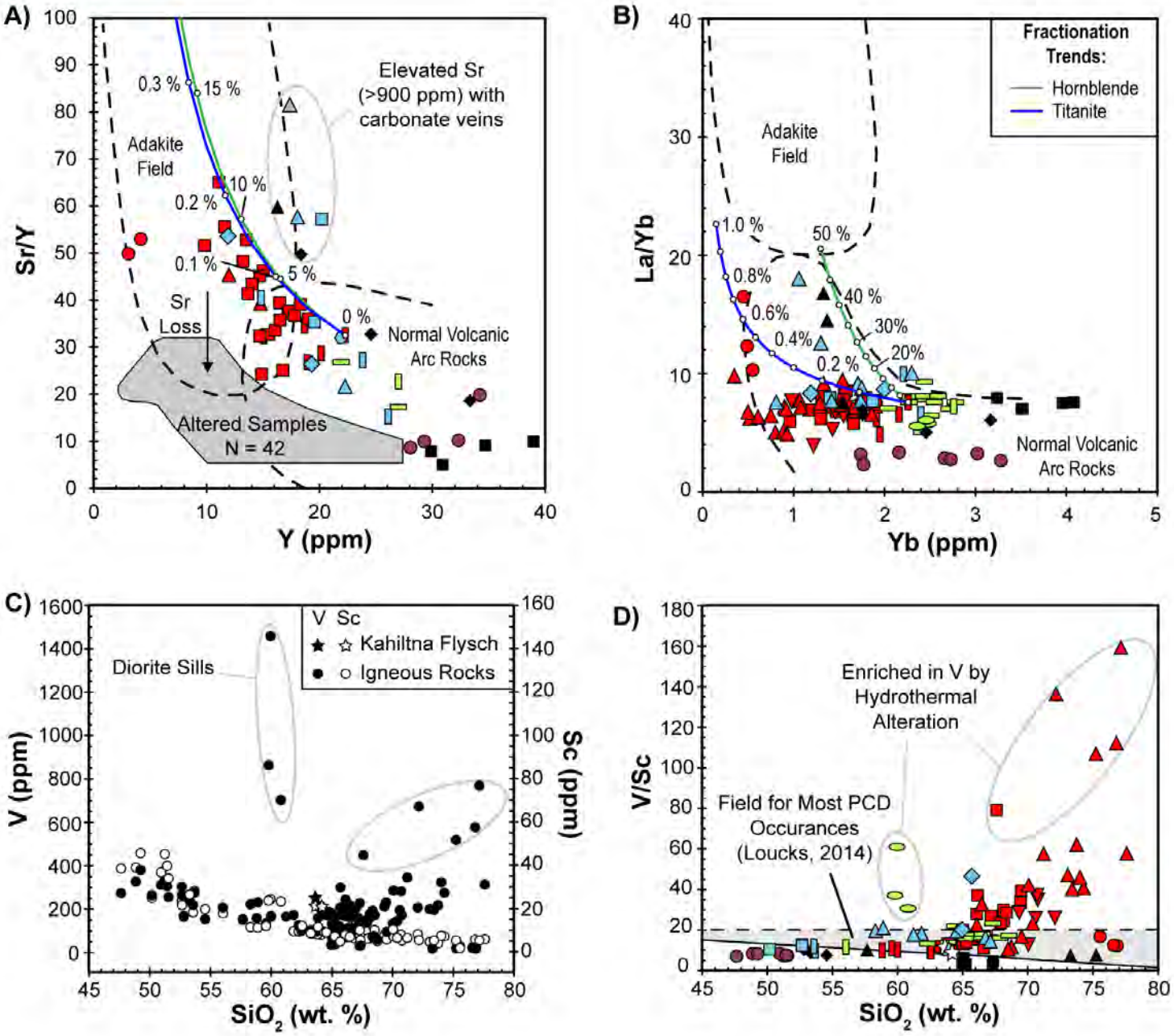

This is a preprint, the final version is subject to change, of the American Mineralogist (MSA)
Cite as Authors (Year) Title. American Mineralogist, in press.
(DOI will not work until issue is live.) DOI: http://dx.doi.org/10.2138/am-2017-6053

Figure 08

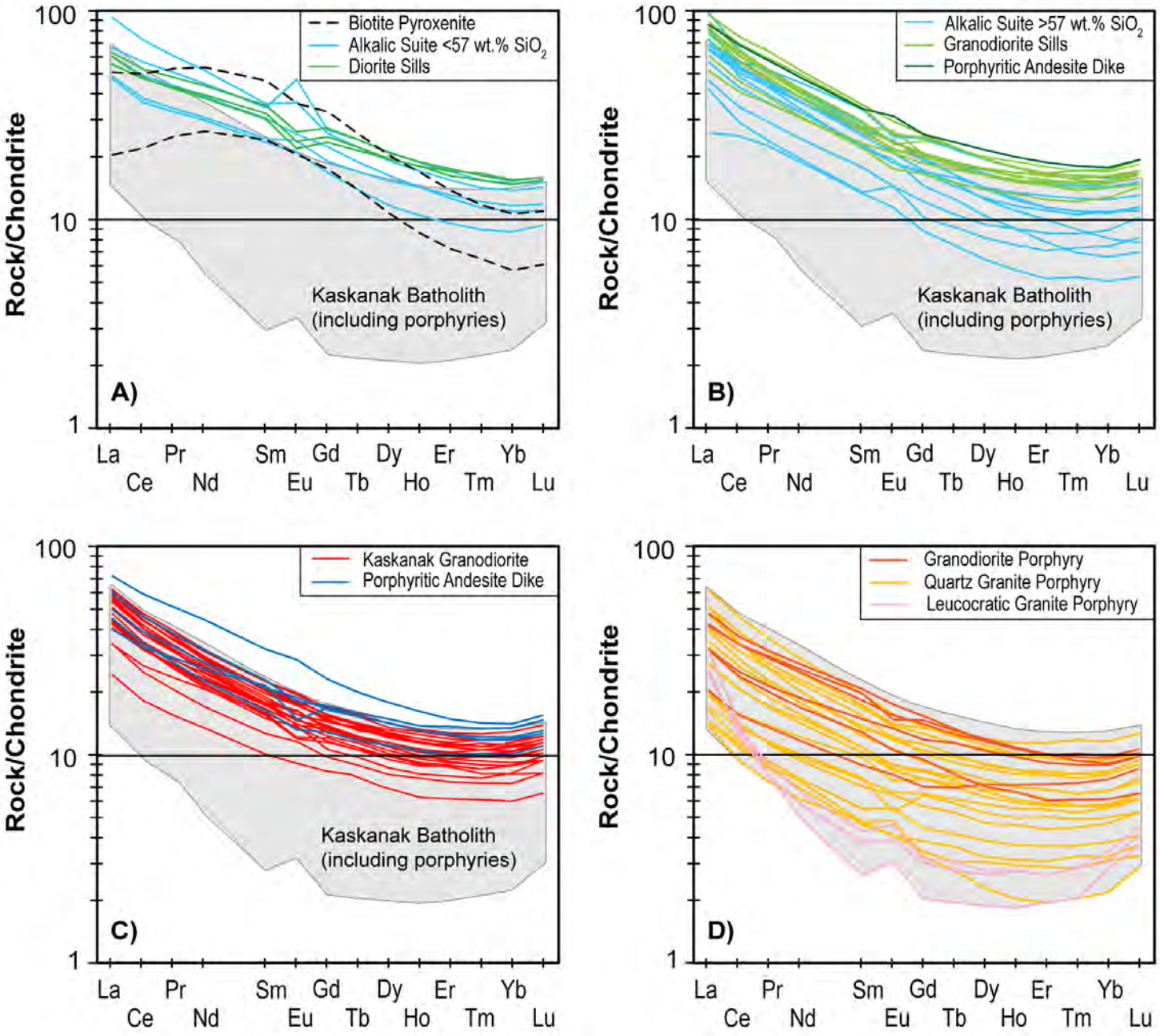

This is a preprint, the final version is subject to change, of the American Mineralogist (MSA)
Cite as Authors (Year) Title. American Mineralogist, in press.
(DOI will not work until issue is live.) DOI: http://dx.doi.org/10.2138/am-2017-6053

Figure 09

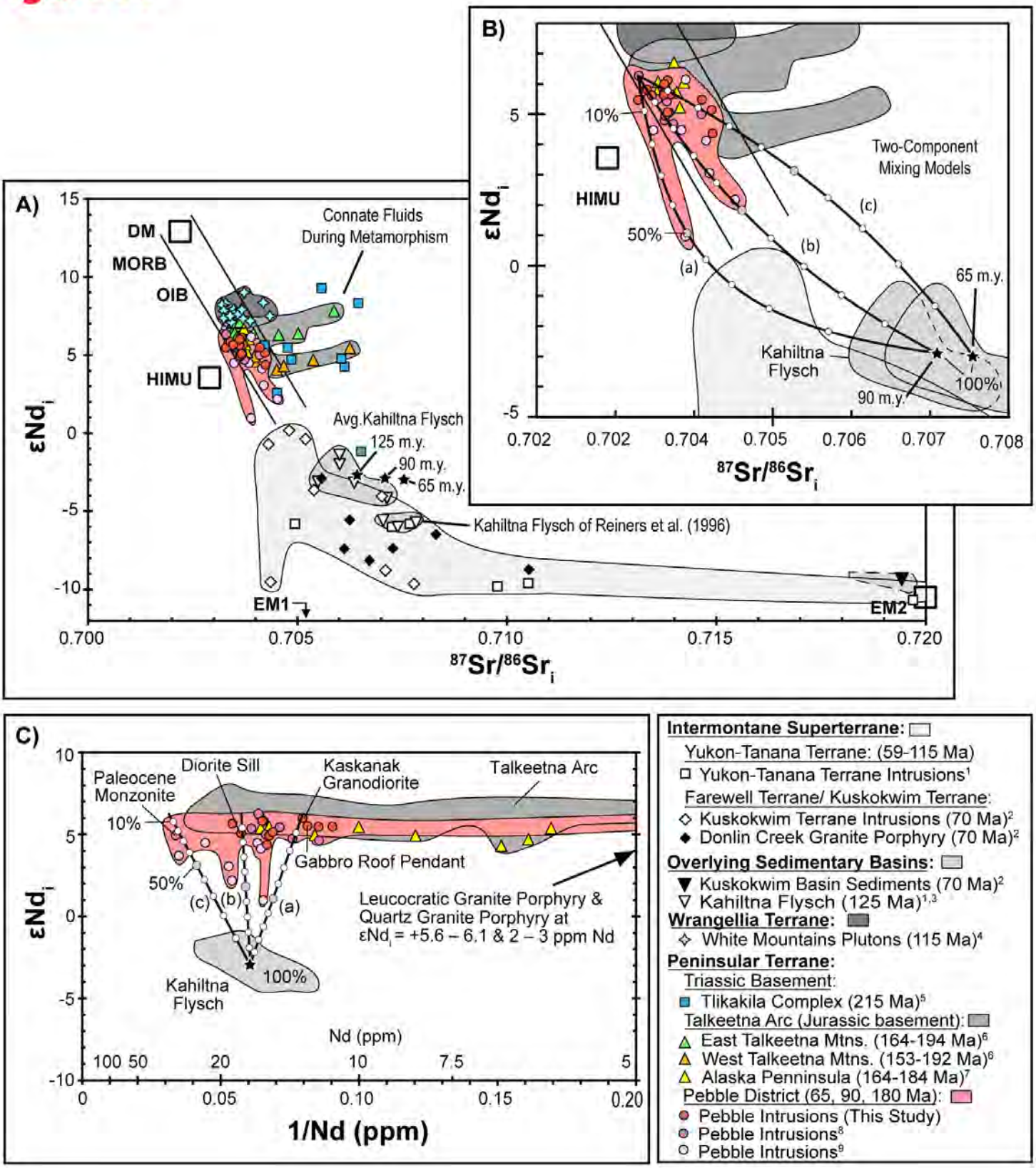

This is a preprint, the final version is subject to change, of the American Mineralogist (MSA)
Cite as Authors (Year) Title. American Mineralogist, in press.
(DOI will not work until issue is live.) DOI: http://dx.doi.org/10.2138/am-2017-6053

Figure 10

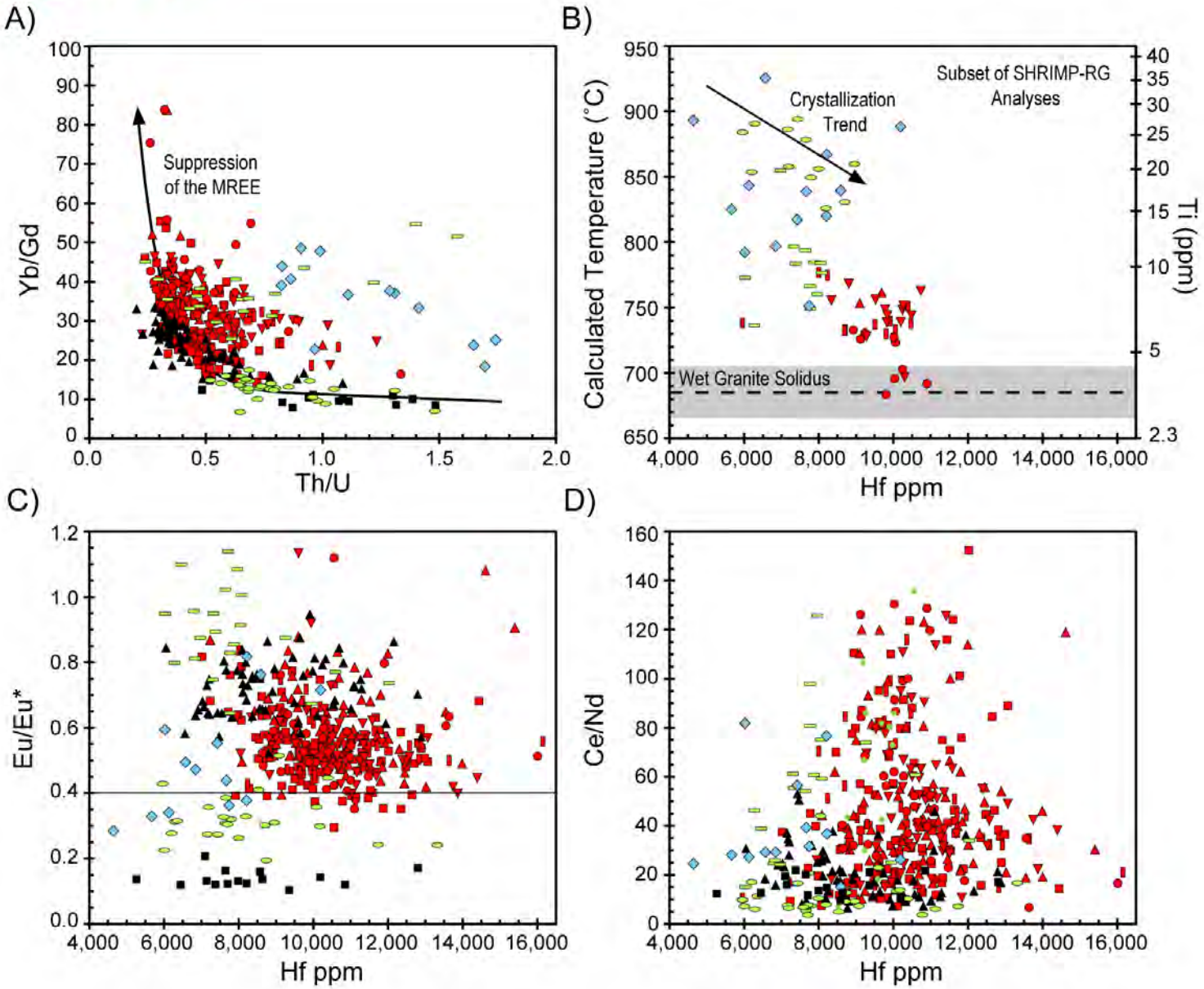

This is a preprint, the final version is subject to change, of the American Mineralogist (MSA)
Cite as Authors (Year) Title. American Mineralogist, in press.
(DOI will not work until issue is live.) DOI: http://dx.doi.org/10.2138/am-2017-6053

Figure 11

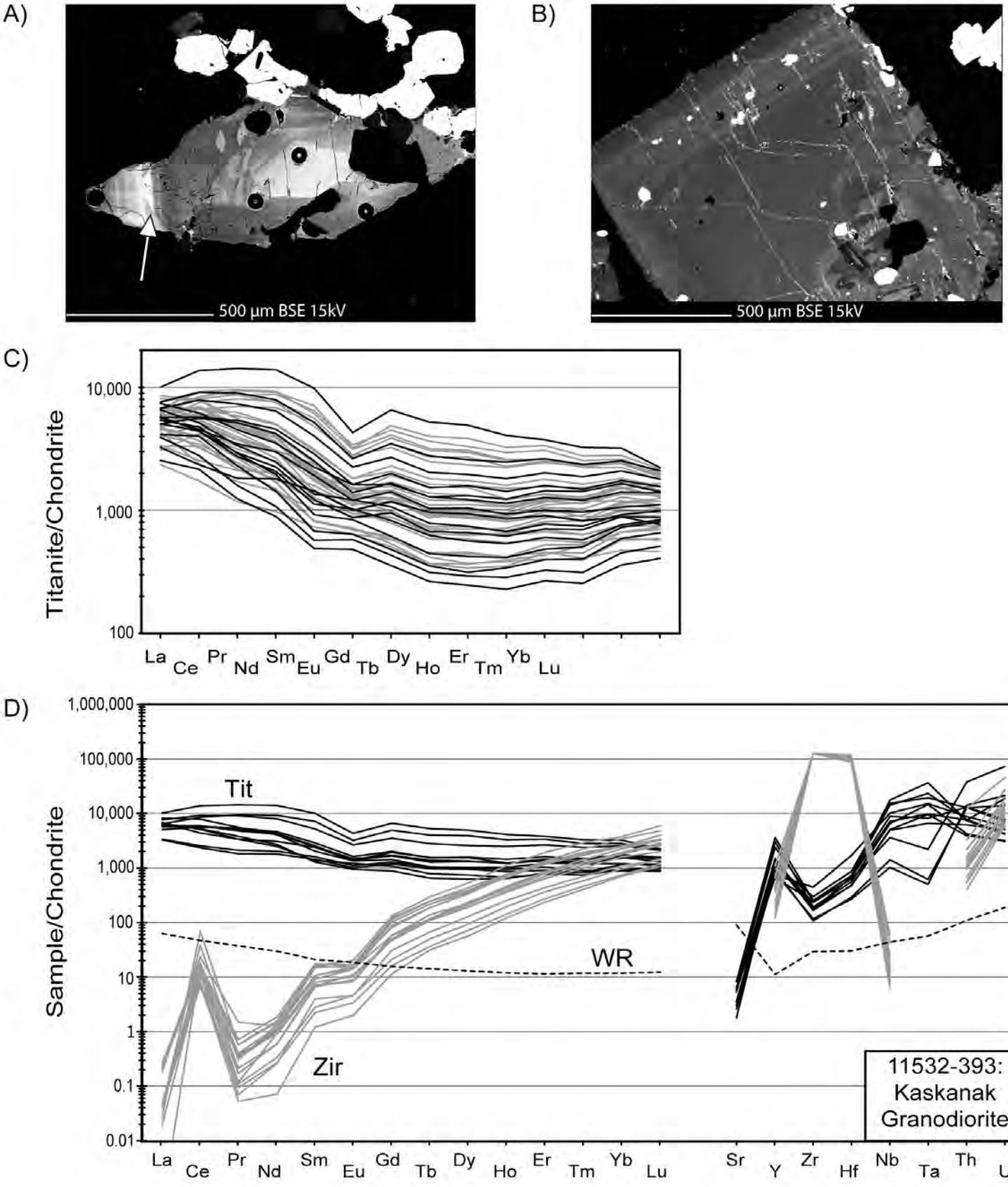

This is a preprint, the final version is subject to change, of the American Mineralogist (MSA)
Cite as Authors (Year) Title. American Mineralogist, in press.
(DOI will not work until issue is live.) DOI: http://dx.doi.org/10.2138/am-2017-6053

Figure 12

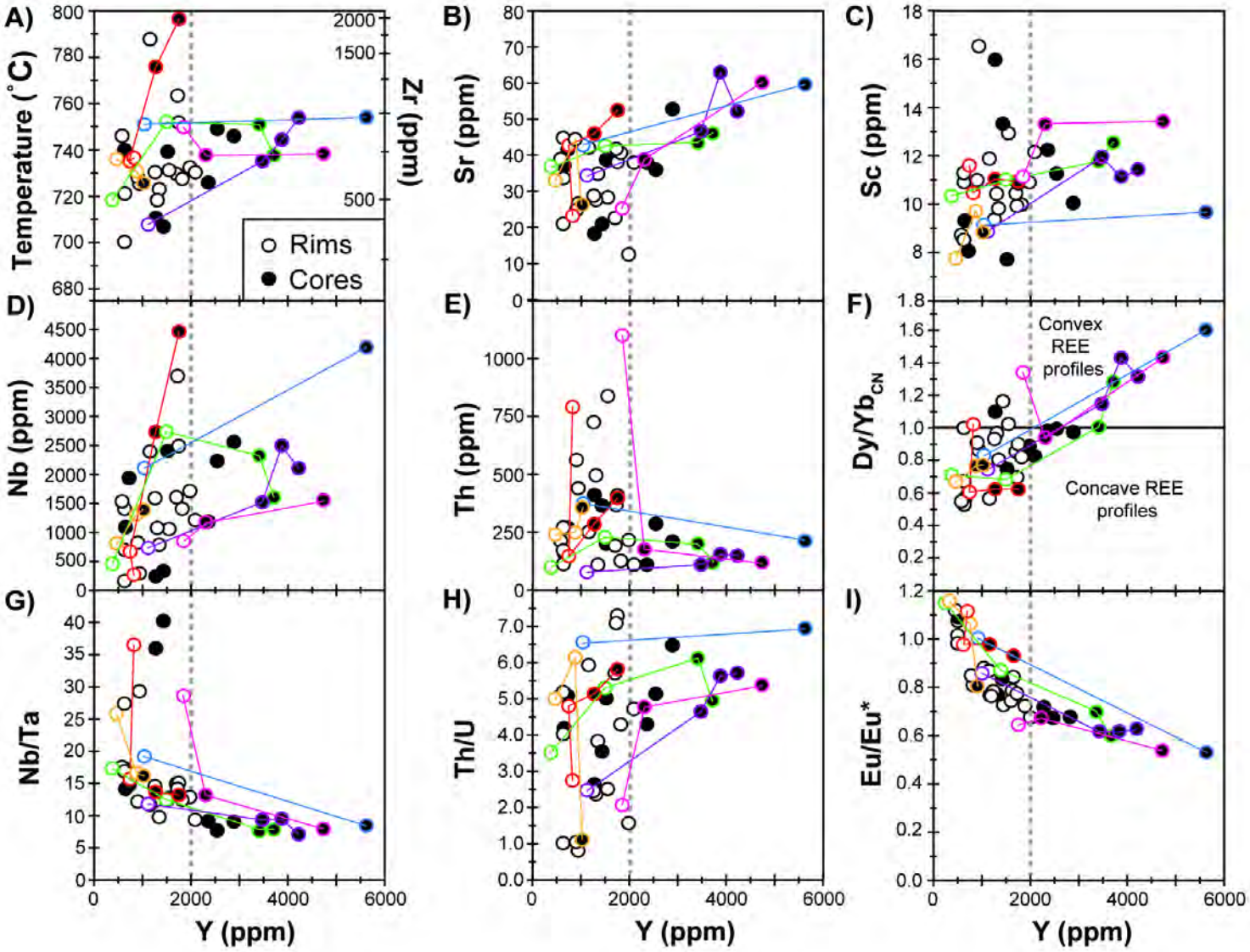

This is a preprint, the final version is subject to change, of the American Mineralogist (MSA)
Cite as Authors (Year) Title. American Mineralogist, in press.
(DOI will not work until issue is live.) DOI: http://dx.doi.org/10.2138/am-2017-6053

Figure 13

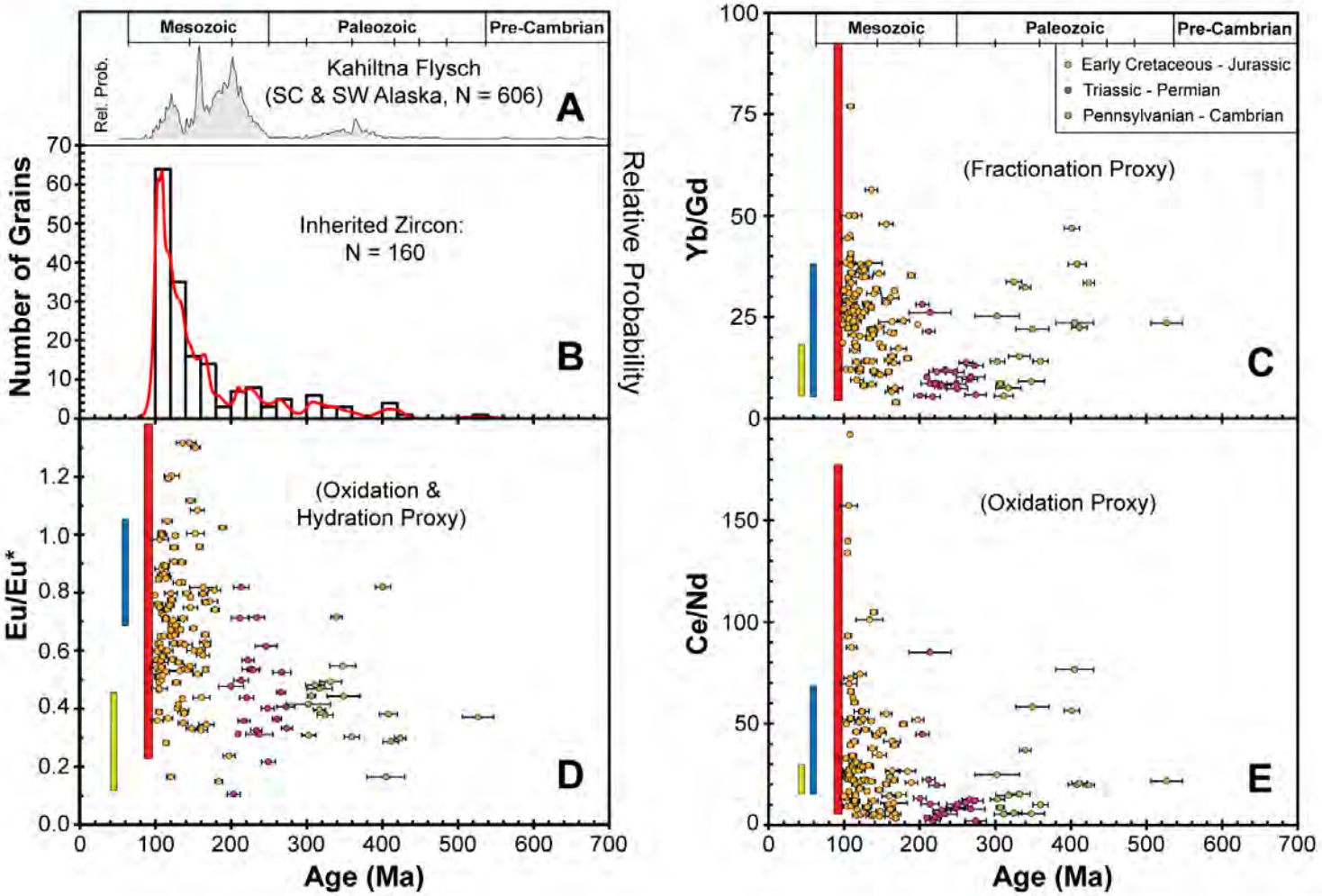

This is a preprint, the final version is subject to change, of the American Mineralogist (MSA)
Cite as Authors (Year) Title. American Mineralogist, in press.
(DOI will not work until issue is live.) DOI: http://dx.doi.org/10.2138/am-2017-6053

Figure 14